JFM PAPERS

Internal tides and the inviscid dynamics of an oscillating ellipsoid in a stratified fluid

Bruno Voisin†

Laboratoire des Écoulements Géophysiques et Industriels, Université Grenoble Alpes, CNRS, Grenoble INP, 38000 Grenoble, France

A boundary integral representation is derived for the translational oscillations of a triaxial ellipsoid in a uniformly stratified fluid. The representation is of single-layer type, a distribution of sources and sinks over the surface of the ellipsoid. The added mass tensor of the ellipsoid is deduced from it and, from this tensor, the impulse response function together with the energy radiated away as internal waves. Horizontal oscillations correspond to the generation of an internal or baroclinic tide by the oscillation of the barotropic tide over ellipsoidal topography at the bottom of the stratified ocean. Such topography is unconditionally supercritical, namely of slope larger than the slope of the wave rays, irrespective of the frequency of oscillation. So far, analytical work on supercritical topographies has been limited, for the most part, to two-dimensional set-ups. Here, for the ellipsoidal seamount, the orientation of the barotropic tide and the anisotropy of the topography have their effects analysed in detail. As the height of the seamount increases, the rate of conversion of barotropic energy into baroclinic form is seen to first increase according to the square law expected for a topography of small slope, then saturate and eventually decrease.

Key words: internal waves, stratified flows, topographic effects

1. Introduction

Internal or baroclinic tides are an important natural manifestation of internal waves, generated by the oscillation of the barotropic tide over topography at the bottom of the ocean (Vlasenko, Stashchuk & Hutter 2005; Morozov 2018). The dissipation of internal tides into turbulence is now believed to play a significant role in ocean mixing and, therefore, affect the climate (St. Laurent & Garrett 2002; Wunsch & Ferrari 2004; Garrett & Kunze 2007; Ferrari & Wunsch 2009; Ferrari *et al.* 2016; Sarkar & Scotti 2017;

† Email address for correspondence: bruno.voisin@cnrs.fr

Whalen *et al.* 2020). In that context, a relevant quantity is the radiated wave power, representing the rate of conversion of barotropic energy into baroclinic form.

The most flexible theoretical approach of the conversion is based on the weak-topography approximation, namely the assumption that the topographic slope is much smaller than the slope of the wave rays, set by the frequency. On this assumption, the bottom boundary condition may be applied at a fictitious flat ocean bottom (Cox & Sandstrom 1962; Bell 1975a,b; Llewellyn Smith & Young 2002; Khatiwala 2003; Bühler & Muller 2007). For barotropic oscillation at the velocity $(U, V) \exp(-i\omega t)$ over a topography of height $h(x, y)$ above the bottom $z = 0$ of a semi-infinite uniformly stratified ocean of density ρ_0 and buoyancy frequency N, with $\omega < N$, the conversion rate follows as

$$P = \frac{\rho_0(N^2 - \omega^2)^{1/2}}{8\pi^2} \iint \frac{(Uk_x + Vk_y)^2}{(k_x^2 + k_y^2)^{1/2}} |h(k_x, k_y)|^2 \, dk_x \, dk_y, \tag{1.1}$$

with

$$h(k_x, k_y) = \iint h(x, y) \exp(-ik_x x - ik_y y) \, dx \, dy, \tag{1.2}$$

or equivalently

$$P = \frac{\rho_0(N^2 - \omega^2)^{1/2}}{4\pi} \iint dx \, dy \left(U\frac{\partial}{\partial x} + V\frac{\partial}{\partial y} \right) h(x, y)$$
$$\times \iint \frac{dx' \, dy'}{[(x - x')^2 + (y - y')^2]^{1/2}} \left(U\frac{\partial}{\partial x'} + V\frac{\partial}{\partial y'} \right) h(x', y'). \tag{1.3}$$

The formulae used in practice account for the elliptic polarization of the barotropic tide (so that U and V are no longer in phase), its finite excursion (so that $(U^2 + V^2)^{1/2}/\omega$ is no longer small compared with the width of the topography), the finite depth of the ocean and the vertical structure of its stratification (so that the waves decompose into vertical modes) and the rotation of the Earth.

Nycander (2005), who derived the convolution integral (1.3), allowing a local computation of the conversion, applied it to the calculation of the total conversion over the global ocean. Later, based on the study of a vertical knife edge by Llewellyn Smith & Young (2003), he pointed out that this integral, giving a conversion rate proportional to the square of the topographic height, overestimated this rate for supercritical slopes, namely slopes larger than that, $\omega/(N^2 - \omega^2)^{1/2}$, of the wave rays (Nycander 2006). Such saturation was accounted for, in the calculations of the global conversion by Green & Nycander (2013), Melet *et al.* (2013), Falahat *et al.* (2014) and Vic *et al.* (2019), by dividing the contribution of each supercritical topography by the square of the ratio of its maximum slope to the ray slope, then capping the outcome at 1 W m^{-2}. As a result, the prediction of the global conversion decreased by 20 % to 30 %.

Other theories exist that do not rely on the weak-topography approximation. In rough chronological order, the first theory uses mode matching for step changes of the ocean depth or bottom slope (Rattray, Dworski & Kovala 1969; Prinsenberg, Wilmot & Rattray 1974; Prinsenberg & Rattray 1975; Stigebrandt 1980; St. Laurent *et al.* 2003), and mode coupling for continuous changes (Griffiths & Grimshaw 2007; Maugé & Gerkema 2008; Papoutsellis, Mercier & Grisouard 2023). Another theory is based on characteristics and represents the barotropic tide either as a body force (Baines 1973, 1974, 1982; Garrett & Gerkema 2007) or a bottom boundary condition (Sandstrom 1976; Craig 1987; Vlasenko 1987; Vlasenko & Cherkesov 1990; Vlasenko *et al.* 2005, chapter 2), with the

potential to lead to functional equations (Dai *et al.* 2011; Maas 2011; Wunsch & Wunsch 2022). A third theory assumes the topography to be subcritical and periodic (Balmforth, Ierley & Young 2002). A fourth theory implements the boundary integral method, either analytically (Gabov & Krutitskii 1987; Krutitskii 1988; Llewellyn Smith & Young 2003) or numerically (Pétrélis, Llewellyn Smith & Young 2006; Balmforth & Peacock 2009; Echeverri & Peacock 2010; Mathur, Carter & Peacock 2016). The predictions of the global conversion by Sjöberg & Stigebrandt (1992) and Gustafsson (2001) use the modal approach, and the predictions by Baines (1982) and Morozov (1995, 2006, 2018, chapter 8) the method of characteristics.

All these approaches, save the weak-topography approximation, assume the topography to be two-dimensional; that is, an infinite ridge, not an isolated seamount. The only exception to this rule is the study of a vertical pillbox by Baines (2007), using mode matching.

Experimental and numerical investigations have been performed as well. Experimentally, the topography is mounted on an oscillating base plate at the top or bottom of a stratified tank. Numerically, both in-house codes have been used and general-purpose codes, either coming from the turbulence community such as CDP, or coming from the oceanographic community such as the Princeton ocean model (POM), the regional ocean modelling system (ROMS) and the MIT global circulation model (MITgcm). These codes differ by their numerical schemes, their adoption of the hydrostatic approximation, of a turbulence model, and their treatment of the bottom boundary using terrain-following coordinates or immersed boundaries. Either experimentally or numerically, two-dimensional ridges with flat tops (Lamb 2004; Tabaei, Akylas & Lamb 2005; Korobov & Lamb 2008), or with polynomial (Di Lorenzo, Young & Llewellyn Smith 2006), Gaussian (Legg & Huijts 2006; Legg & Klymak 2008; Peacock, Echeverri & Balmforth 2008; Echeverri *et al.* 2009; Dossmann *et al.* 2011; Floor, Auclair & Marsaleix 2011; Wang *et al.* 2018), triangular (Dettner, Swinney & Paoletti 2013; Rapaka, Gayen & Sarkar 2013; Jalali, Rapaka & Sarkar 2014; Jia *et al.* 2014; Wang *et al.* 2015; Jalali *et al.* 2017) or circular (Winters & Armi 2013) cross-sections, have all been considered, together with a vertical knife edge (Görtler 1943; Peacock *et al.* 2008; Lee *et al.* 2014). In three dimensions, Gaussian seamounts either axisymmetric (Beckmann & Haidvogel 1993; Haidvogel *et al.* 1993; King, Zhang & Swinney 2010; Zhang *et al.* 2017) or not (Holloway & Merrifield 1999; Munroe & Lamb 2005) have been considered.

Another set-up, introduced for internal waves but applied later to internal tides, consists in oscillating a vertically symmetric body horizontally in a stratified tank. The horizontal midplane through the body acts as the rigid ocean bottom. A horizontal circular cylinder (Mowbray & Rarity 1967; Thomas & Stevenson 1972; Peters 1985; Zhang, King & Swinney 2007; Ermanyuk & Gavrilov 2008), a sphere (King, Zhang & Swinney 2009; Ermanyuk, Flór & Voisin 2011; Voisin, Ermanyuk & Flór 2011) and a prolate spheroid with vertical or horizontal axis (Shmakova, Ermanyuk & Flór 2017) have been studied in this way.

A prominent feature of these investigations is the presence, when $\omega < N/2$, of a second harmonic wave of frequency 2ω. The fundamental wave propagates at the angle $\arccos(\omega/N)$ to the vertical, and the second harmonic at the angle $\arccos(2\omega/N)$. Also present, for three-dimensional set-ups, is a transverse mean flow. Theoretically, as discussed by Zhang *et al.* (2007) and Ermanyuk *et al.* (2011), two mechanisms can produce a second harmonic: for barotropic excursion larger than the horizontal size of the topography, the dominant mechanism is advection of the boundary forcing; for smaller excursion, the dominant mechanism is the interaction of the wave rays emanating from the topography, either within themselves, or with the rays reflected at the bottom and the

surface, or with the boundary layer. Consistent with this analysis, the second harmonic rays visible in the experiments by Zhang *et al.* (2007), and the simulations by Tabaei *et al.* (2005) and Korobov & Lamb (2008), all with supercritical topographies, are seen to emanate from the points where the critical rays (or their reflections) either intersect themselves or are tangential to the topography.

Therefore, the modelling of a second harmonic wave requires prior understanding of the fundamental wave and of the boundary layer. The circular cylinder and the sphere, used in the laboratory, exhibit the interesting property of being always supercritical. Accordingly, critical rays always exist that are tangential to them. To vary the curvature at the points of tangency, and hence the local structure of the boundary layer, Shmakova *et al.* (2017) switched to a spheroid. In this respect, Sutherland & Linden (2002), who had considered the vertical oscillations of a horizontal elliptic cylinder, had acted as a precursor. Both investigations were experimental. In a rotating fluid, for the similar inertial waves, Le Dizès & Le Bars (2017) considered a librating spheroid of vertical axis, numerically and theoretically. Using local analysis for generic two-dimensional boundary forcing, Le Dizès (2024) pointed out, for both internal and inertial waves, a dependence of the wave amplitude on the curvature of the boundary at the critical points.

The present paper is a follow-up to the application of the boundary integral method to the oscillations of an elliptic cylinder and a spheroid by Voisin (2021), and to the interpretation of the outcome in terms of added mass by Voisin (2024). The analysis is extended here to a triaxial ellipsoid, with the same limitation to translational motions. Given the complexity of the analysis, the presentation of the background is kept to a minimum and the reader is referred to Voisin (2021, 2024) for details. The waves, to be compared with the observations of Shmakova *et al.* (2017), are not calculated at this stage. The calculation will arise later, by extension of the two-dimensional approach of Voisin (2020) to three dimensions. For now, attention is focused on added mass and its consequences, regarding the force acting on the ellipsoid and the energy radiated away from it. For horizontal oscillations, the conversion rate is obtained for barotropic tidal flow over ellipsoidal topography at the bottom of a semi-infinite uniformly stratified ocean.

Mathematically, the exposition relies on the presentation of ellipsoidal harmonics by Dassios (2012), with one additional result taken from Hobson (1931, chapter 11). The relevant formulae are gathered in Appendix A. Section 2 develops the approach for the potential flow of a homogeneous fluid, obtaining the added mass tensor of the ellipsoid and comparing it with the literature. Section 3 extends this approach to the oscillations of the ellipsoid in a stratified fluid. Particular attention is paid to the transition from three to two dimensions, namely from a spheroid to an elliptic cylinder, which are both limits of the ellipsoid. Section 4 deduces the memory force exerted on a moving ellipsoid, expressed in terms of its impulse response function, together with the power radiated away from an oscillating ellipsoid. Section 5 investigates the conversion rate of ellipsoidal topography. The results are compared with the literature, either analytical (Llewellyn Smith & Young 2002) or numerical (Munroe & Lamb 2005), in both cases for Gaussian topography. The effects of the weak-topography approximation used by Llewellyn Smith & Young (2002), and of the supercritical correction introduced by Green & Nycander (2013), Melet *et al.* (2013), Falahat *et al.* (2014) and Vic *et al.* (2019), are discussed in detail. The main conclusions are summarized in § 6.

2. Homogeneous fluid

A body of surface S and outward normal $\boldsymbol{n}$, moving at the velocity $\boldsymbol{U}$ in a homogeneous fluid, generates an irrotational flow of potential ϕ and velocity $\boldsymbol{u} = \nabla\phi$, with ∇ the

del operator. The potential satisfies the Laplace equation

$$\nabla^2 \phi = 0, \tag{2.1}$$

together with the boundary condition

$$\frac{\partial \phi}{\partial n} = U_n \quad (\boldsymbol{x} \in S_+), \tag{2.2}$$

where $\partial/\partial n = \boldsymbol{n} \cdot \boldsymbol{\nabla}$ denotes the normal derivative, $U_n = \boldsymbol{n} \cdot \boldsymbol{U}$ the normal velocity, $\boldsymbol{x}$ the position and S_+ the side of S in contact with the fluid.

2.1. *Representation*

We look for a representation of the body as the single layer, namely the surface distribution of sources and sinks,

$$q(\boldsymbol{x}) = \boldsymbol{\nabla} \cdot \boldsymbol{u} = \sigma(\boldsymbol{x})\delta_S(\boldsymbol{x}), \tag{2.3}$$

with δ_S the Dirac delta function of support S. This distribution appears as a source term on the right-hand side of (2.1) and generates the potential

$$\phi(\boldsymbol{x}) = -\frac{1}{4\pi} \int_S \frac{\sigma(\boldsymbol{x}')}{|\boldsymbol{x} - \boldsymbol{x}'|} \, \mathrm{d}^2 S'. \tag{2.4}$$

The boundary condition is turned into an integro-differential equation

$$U_n(\boldsymbol{x}) = -\frac{1}{4\pi} \frac{\partial}{\partial n} \int_S \frac{\sigma(\boldsymbol{x}')}{|\boldsymbol{x} - \boldsymbol{x}'|} \, \mathrm{d}^2 S' \quad (\boldsymbol{x} \in S_+), \tag{2.5}$$

to be solved for the layer density σ given the normal velocity U_n.

The body is taken to be a triaxial ellipsoid of semi-axes $a > b > c$, represented in figure 1, with

$$\frac{x^2}{a^2} + \frac{y^2}{b^2} + \frac{z^2}{c^2} = 1 \tag{2.6}$$

in Cartesian coordinates (x, y, z). We introduce the ellipsoidal coordinates (ρ, μ, ν), defined in (A3). The ellipsoid becomes the surface $\rho = a$, and the boundary condition becomes

$$U_n(\mu, \nu) = -\frac{bc}{4\pi} \frac{\partial}{\partial \rho} \int_{\rho'=a} \frac{\sigma(\mu', \nu')}{|\boldsymbol{x} - \boldsymbol{x}'|} \frac{(a^2 - \mu'^2)^{1/2}(a^2 - \nu'^2)^{1/2}}{(a^2 - \mu^2)^{1/2}(a^2 - \nu^2)^{1/2}} \, \mathrm{d}\varpi' \quad (\rho = a + 0), \tag{2.7}$$

with $\mathrm{d}\varpi$ the solid angle element (A8). Further introduction of the eccentric angles (ϑ, φ), related to (μ, ν) by (A9), parametrizes the ellipsoid as

$$x = a \cos \vartheta, \quad y = b \sin \vartheta \cos \varphi, \quad z = c \sin \vartheta \sin \varphi, \tag{2.8a–c}$$

with $0 < \vartheta < \pi$ and $0 < \varphi < 2\pi$, transferring the integration onto the unit sphere, with solid angle element $\mathrm{d}\varpi = \sin \vartheta \, \mathrm{d}\vartheta \, \mathrm{d}\varphi$. The boundary condition becomes

$$U_n(\mu, \nu) = -\frac{bc}{4\pi} \frac{\partial}{\partial \rho} \int_0^{2\pi} \int_0^{\pi} \frac{\sigma(\mu', \nu')}{|\boldsymbol{x} - \boldsymbol{x}'|} \frac{(a^2 - \mu'^2)^{1/2}(a^2 - \nu'^2)^{1/2}}{(a^2 - \mu^2)^{1/2}(a^2 - \nu^2)^{1/2}} \sin \vartheta' \, \mathrm{d}\vartheta' \, \mathrm{d}\varphi', \tag{2.9}$$
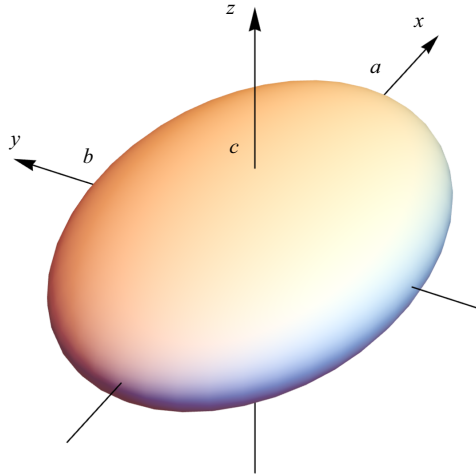
where $\rho' = a$ and $\rho = a + 0$.

Figure 1. Ellipsoid of aspect ratios $\epsilon_1 = c/b = 1/2$ and $\epsilon_3 = b/a = 2/3$.

The problem is solved in ellipsoidal harmonics, combining the Lamé functions $E_l^m(\rho)$, the elliptic integrals $I_l^m(\rho)$ and the surface harmonics $s_l^m(\vartheta, \varphi)$, presented in §§ A.2 and A.3, with the degree l taking the values $0, 1, 2, \ldots$ and the index m the values $1, 2, \ldots, 2l + 1$. The known $U_n(\mu, \nu)$ is expanded as

$$(a^2 - \mu^2)^{1/2}(a^2 - \nu^2)^{1/2}U_n(\mu, \nu) = \sum_{l=0}^{\infty} \sum_{m=1}^{2l+1} U_{lm}s_l^m(\vartheta, \varphi), \tag{2.10}$$

and the unknown $\sigma(\mu, \nu)$ as

$$(a^2 - \mu^2)^{1/2}(a^2 - \nu^2)^{1/2}\sigma(\mu, \nu) = \sum_{l=0}^{\infty} \sum_{m=1}^{2l+1} \sigma_{lm}s_l^m(\vartheta, \varphi). \tag{2.11}$$

Expansion (A37) of the kernel $1/|\boldsymbol{x} - \boldsymbol{x}'|$ yields, for $\rho' = a$ and $\rho = a + 0$,

$$\frac{\partial}{\partial \rho} \frac{1}{|\boldsymbol{x} - \boldsymbol{x}'|} = -\frac{4\pi}{bc} \sum_{l=0}^{\infty} \sum_{m=1}^{2l+1} [1 - bcE_l^m(a)E_l^{m\,\prime}(a)I_l^m(a)]s_l^m(\vartheta, \varphi)s_l^m(\vartheta', \varphi'). \tag{2.12}$$

In view of the orthonormality relation (A31), we obtain

$$\sigma_{lm} = \frac{U_{lm}}{1 - bcE_l^m(a)E_l^{m\,\prime}(a)I_l^m(a)}, \tag{2.13}$$

and the representation of the ellipsoid follows as

$$q(\boldsymbol{x}) = \frac{1}{abc}\delta\left[\left(\frac{x^2}{a^2} + \frac{y^2}{b^2} + \frac{z^2}{c^2}\right)^{1/2} - 1\right] \sum_{l=0}^{\infty} \sum_{m=1}^{2l+1} \sigma_{lm}s_l^m(\vartheta, \varphi), \tag{2.14}$$

with δ the Dirac delta function.

999 A59-6

2.2. *Spectrum*

The spectrum

$$q(\boldsymbol{k}) = \int_S \sigma(\boldsymbol{x}) \exp(-\mathrm{i}\boldsymbol{k} \cdot \boldsymbol{x}) \, \mathrm{d}^2 S \tag{2.15}$$

is also of interest, with later application to waves in mind. We note for now that the source and dipole strengths

$$\mathcal{S} = \int_S \sigma(\boldsymbol{x}) \, \mathrm{d}^2 S, \quad \boldsymbol{\mathcal{D}} = \int_S \boldsymbol{x}\sigma(\boldsymbol{x}) \, \mathrm{d}^2 S, \tag{2.16a,b}$$

respectively, may be deduced from the small-wavenumber expansion

$$q(\boldsymbol{k}) \sim \mathcal{S} - \mathrm{i}\boldsymbol{k} \cdot \boldsymbol{\mathcal{D}}. \tag{2.17}$$

We thus need to calculate the integral

$$q(\boldsymbol{k}) = \sum_{l=0}^{\infty} \sum_{m=1}^{2l+1} \sigma_{lm} \int_0^{2\pi} \int_0^{\pi} \exp(-\mathrm{i}\boldsymbol{k} \cdot \boldsymbol{x}) s_l^m(\vartheta, \varphi) \sin\vartheta \, \mathrm{d}\vartheta \, \mathrm{d}\varphi, \tag{2.18}$$

where $\boldsymbol{x}$ is related to (ϑ, φ) by (2.8).

In spherical geometry, the natural basis for expanding a function of the spherical angles (ϑ, φ) is the surface harmonics

$$Y_l^n(\vartheta, \varphi) = \sqrt{\frac{2l+1}{4\pi} \frac{(l-n)!}{(l+n)!}} \, \mathrm{P}_l^n(\cos\vartheta) \exp(\mathrm{i}n\varphi), \tag{2.19}$$

with P_l^n an associated Legendre function, of degree $l = 0, 1, 2, \dots$ and order $n = -l, -l + 1, \dots, l - 1, l$. See for example Jackson (1999, § 3.5). Then, Gegenbauer's finite integral

$$\int_0^{\pi} \exp(\mathrm{i}\kappa \cos\vartheta \cos\vartheta_k) \, \mathrm{J}_n(\kappa \sin\vartheta \sin\vartheta_k) \, \mathrm{P}_l^n(\cos\vartheta) \sin\vartheta \, \mathrm{d}\vartheta = 2\mathrm{i}^{l-n} \, \mathrm{j}_l(\kappa) \, \mathrm{P}_l^n(\cos\vartheta_k), \tag{2.20}$$

derived by Watson (1944, § 12.14), where J_n denotes a cylindrical Bessel function and j_l a spherical Bessel function, leads to the Funk–Hecke formula

$$\int_0^{2\pi} \int_0^{\pi} \exp(-\mathrm{i}\boldsymbol{k} \cdot \boldsymbol{x}) Y_l^n(\vartheta, \varphi) \sin\vartheta \, \mathrm{d}\vartheta \, \mathrm{d}\varphi = 4\pi(-\mathrm{i})^l \, \mathrm{j}_l(\kappa) Y_l^n(\vartheta_k, \varphi_k), \tag{2.21}$$

with (ϑ_k, φ_k) the spherical angles in Fourier space, such that

$$\boldsymbol{k} \cdot \boldsymbol{x} = \kappa[\cos\vartheta \cos\vartheta_k + \sin\vartheta \sin\vartheta_k \cos(\varphi - \varphi_k)]. \tag{2.22}$$

See for example Martin (2006, § 3.6).

In ellipsoidal geometry, Hobson (1931, §§ 280–281) pointed out that each surface spherical harmonic $Y_l^n(\vartheta, \varphi)$, with (ϑ, φ) the eccentric angles, is a linear combination of the $2l + 1$ ellipsoidal harmonics $s_l^m(\vartheta, \varphi)$ of the same degree l. Conversely, each surface ellipsoidal harmonic $s_l^m(\vartheta, \varphi)$ is a linear combination of the spherical harmonics $Y_l^n(\vartheta, \varphi)$

of the same degree. Accordingly, the Funk–Hecke formula generalizes to ellipsoidal harmonics in the form

$$\int_0^{2\pi} \int_0^{\pi} \exp(-\mathrm{i}\boldsymbol{k} \cdot \boldsymbol{x}) s_l^m(\vartheta, \varphi) \sin \vartheta \, \mathrm{d}\vartheta \, \mathrm{d}\varphi = 4\pi(-\mathrm{i})^l \mathrm{j}_l(\kappa) s_l^m(\vartheta_k, \varphi_k), \tag{2.23}$$

where the angles (ϑ_k, φ_k) are defined in Fourier space by

$$k_x a = \kappa \cos \vartheta_k, \quad k_y b = \kappa \sin \vartheta_k \cos \varphi_k, \quad k_z c = \kappa \sin \vartheta_k \sin \varphi_k, \tag{2.24a–c}$$

with $\kappa = (k_x^2 a^2 + k_y^2 b^2 + k_z^2 c^2)^{1/2}$.

We thus have

$$q(\boldsymbol{k}) = 4\pi \sum_{l=0}^{\infty} (-\mathrm{i})^l \mathrm{j}_l[(k_x^2 a^2 + k_y^2 b^2 + k_z^2 c^2)^{1/2}] \sum_{m=1}^{2l+1} \sigma_{lm} s_l^m(\vartheta_k, \varphi_k), \tag{2.25}$$

generalizing Voisin (2021, (6.28)), obtained for a spheroid.

2.3. *Monopolar motion*

The analysis is applied first to the radial expansion or contraction of the ellipsoid at the velocity $\boldsymbol{U} = U\boldsymbol{x}/(abc)^{1/3}$, with U a constant. Such forcing is of degree $l = 0$, with

$$U_{01} = \sqrt{4\pi} U(abc)^{2/3} = \sigma_{01}. \tag{2.26}$$

It has the representation

$$q(\boldsymbol{x}) = \frac{U}{(abc)^{1/3}} \delta\left[\left(\frac{x^2}{a^2} + \frac{y^2}{b^2} + \frac{z^2}{c^2} \right)^{1/2} - 1 \right] \tag{2.27}$$

and the spectrum

$$q(\boldsymbol{k}) = 4\pi U(abc)^{2/3} \mathrm{j}_0[(k_x^2 a^2 + k_y^2 b^2 + k_z^2 c^2)^{1/2}], \tag{2.28}$$

corresponding to a source of strength $\mathcal{S} = 4\pi U(abc)^{2/3}$.

2.4. *Dipolar motion*

The translation of a rigid ellipsoid at the velocity $\boldsymbol{U} = U\boldsymbol{e}_x + V\boldsymbol{e}_y + W\boldsymbol{e}_z$, with (U, V, W) constants, is of degree $l = 1$, such that

$$U_{11} = \sqrt{\frac{4\pi}{3}} bcU, \quad U_{12} = \sqrt{\frac{4\pi}{3}} acV, \quad U_{13} = \sqrt{\frac{4\pi}{3}} abW. \tag{2.29a–c}$$

The equivalent source has coefficients

$$\sigma_{11} = \frac{U_{11}}{1 - A}, \quad \sigma_{12} = \frac{U_{12}}{1 - B}, \quad \sigma_{13} = \frac{U_{13}}{1 - C}, \tag{2.30a–c}$$

where A, B and C are related to the Legendre integrals (A18) by

$$A = abcI_1^1(a) = \frac{abc}{a^2 - b^2} \frac{F(\alpha, \beta) - E(\alpha, \beta)}{(a^2 - c^2)^{1/2}}, \tag{2.31a}$$

$$B = abcI_1^2(a) = \frac{abc}{a^2 - b^2} \frac{E(\alpha, \beta)/(1 - \beta) - F(\alpha, \beta)}{(a^2 - c^2)^{1/2}} - \frac{c^2}{b^2 - c^2}, \tag{2.31b}$$

$$C = abcI_1^3(a) = \frac{b^2}{b^2 - c^2} - \frac{abc}{b^2 - c^2} \frac{E(\alpha, \beta)}{(a^2 - c^2)^{1/2}}, \tag{2.31c}$$

with

$$\alpha = \arccos\left(\frac{c}{a}\right), \quad \beta = \frac{a^2 - b^2}{a^2 - c^2}. \tag{2.32a,b}$$

These A, B and C are identical to $\alpha_0/2$, $\beta_0/2$ and $\gamma_0/2$, respectively, in Lamb (1932, § 114) and Milne-Thomson (1968, § 17.52), and $A_0/2$, $B_0/2$ and $C_0/2$ in Kochin, Kibel' & Roze (1964, §§ 7.2 and 7.8) and Korotkin (2009, § 3.1), all expressed as gravitational potentials. See also Dassios (2012, § 13.5).

Forcing is of the dipolar type, in direct space

$$q(\boldsymbol{x}) = \left(\frac{U}{1-A}\frac{x}{a^2} + \frac{V}{1-B}\frac{y}{b^2} + \frac{W}{1-C}\frac{z}{c^2}\right)\delta\left[\left(\frac{x^2}{a^2} + \frac{y^2}{b^2} + \frac{z^2}{c^2}\right)^{1/2} - 1\right], \tag{2.33}$$

and in Fourier space

$$q(\boldsymbol{k}) = -4i\pi abc\left(\frac{Uk_x}{1-A} + \frac{Vk_y}{1-B} + \frac{Wk_z}{1-C}\right)\frac{j_1[(k_x^2 a^2 + k_y^2 b^2 + k_z^2 c^2)^{1/2}]}{(k_x^2 a^2 + k_y^2 b^2 + k_z^2 c^2)^{1/2}}, \tag{2.34}$$

with strength

$$\boldsymbol{\mathcal{D}} = \frac{4}{3}\pi abc\left(\frac{U}{1-A}\boldsymbol{e}_x + \frac{V}{1-B}\boldsymbol{e}_y + \frac{W}{1-C}\boldsymbol{e}_z\right). \tag{2.35}$$

The bodies considered by Voisin (2021, 2024) are recovered as particular cases. These include: the oblate spheroid, for which

$$A = B = \frac{1 - D(\epsilon)}{2}, \quad C = D(\epsilon) = \frac{1}{1-\epsilon^2}\left[1 - \frac{\epsilon\arccos\epsilon}{(1-\epsilon^2)^{1/2}}\right], \tag{2.36a,b}$$

where $\epsilon = c/a < 1$, corresponding to $a = b$, namely $\beta \to 0$; the prolate spheroid, for which

$$A = D(\epsilon) = \frac{1}{1-\epsilon^2}\left[1 - \frac{\epsilon\,\text{arccosh}\,\epsilon}{(\epsilon^2-1)^{1/2}}\right], \quad B = C = \frac{1 - D(\epsilon)}{2}, \tag{2.37a,b}$$

where $\epsilon = a/b > 1$, corresponding to $b = c$, namely $\beta \to 1$; and the elliptic cylinder, for which

$$A = 0, \quad B = \frac{\epsilon}{1+\epsilon}, \quad C = \frac{1}{1+\epsilon}, \tag{2.38a–c}$$

where $\epsilon = c/b < 1$, corresponding to $a \to \infty$, namely $(\alpha, \beta) \to (\pi/2, 1)$. More specific cases are the sphere, for which

$$A = B = C = \tfrac{1}{3}, \tag{2.39}$$

corresponding to $a = b = c$, and the circular cylinder, for which

$$A = 0, \quad B = C = \tfrac{1}{2}, \tag{2.40a,b}$$

corresponding to $a \to \infty$ and $b = c$.

2.5. *Added mass*

The dynamics of a rigid body in an inviscid fluid is governed by its added mass, representing the additional inertia imparted to it by the motion of the fluid (Batchelor 1967, § 6.4; Lighthill 1986, § 8.3; Landau & Lifshitz 1987, § 11). The added mass tensor of the ellipsoid is diagonal, and the ratios C_x, C_y and C_z of its elements to the mass of the displaced fluid are related to the components $\mathcal{D}_x$, $\mathcal{D}_y$ and $\mathcal{D}_z$ of the dipole strength by

$$C_x = \frac{\mathcal{D}_x}{\mathcal{V}U} - 1, \quad C_y = \frac{\mathcal{D}_y}{\mathcal{V}V} - 1, \quad C_z = \frac{\mathcal{D}_z}{\mathcal{V}W} - 1, \tag{2.41a–c}$$

with $\mathcal{V} = (4/3)\pi abc$ the volume of the ellipsoid. We obtain

$$C_x = \frac{A}{1 - A}, \quad C_y = \frac{B}{1 - B}, \quad C_z = \frac{C}{1 - C}. \tag{2.42a–c}$$

Introducing the aspect ratios $\epsilon_1 = c/b$ and $\epsilon_3 = b/a$, both smaller than 1, we have

$$A(\epsilon_1, \epsilon_3) = \frac{\epsilon_1 \epsilon_3^2}{1 - \epsilon_3^2} \frac{F(\alpha, \beta) - E(\alpha, \beta)}{(1 - \epsilon_1^2 \epsilon_3^2)^{1/2}}, \tag{2.43a}$$

$$B(\epsilon_1, \epsilon_3) = \frac{\epsilon_1 \epsilon_3^2}{1 - \epsilon_3^2} \frac{E(\alpha, \beta)/(1 - \beta) - F(\alpha, \beta)}{(1 - \epsilon_1^2 \epsilon_3^2)^{1/2}} - \frac{\epsilon_1^2}{1 - \epsilon_1^2}, \tag{2.43b}$$

$$C(\epsilon_1, \epsilon_3) = \frac{1}{1 - \epsilon_1^2} - \frac{\epsilon_1}{1 - \epsilon_1^2} \frac{E(\alpha, \beta)}{(1 - \epsilon_1^2 \epsilon_3^2)^{1/2}}, \tag{2.43c}$$

where

$$\alpha = \arccos(\epsilon_1 \epsilon_3), \quad \beta = \frac{1 - \epsilon_3^2}{1 - \epsilon_1^2 \epsilon_3^2}. \tag{2.44a,b}$$

The variations of the added mass coefficients with ϵ_1 and ϵ_3 are plotted in figure 2. They are in agreement with figures 150–152 of Kochin *et al.* (1964) and 3.1–3.2 of Korotkin (2009), representing the variations of the coefficients with ϵ_1 for specific values of $1/\epsilon_3$.

3. Stratified fluid

The analysis is now adapted to linear internal waves in a uniformly stratified fluid of buoyancy frequency N. The formulation is based on Voisin (2021, 2024), to which the reader is referred for further detail. The waves are assumed to vary with time through the factor $\exp(-i\omega t)$, which is suppressed in the following, and to be analytic in the upper half of the complex ω-plane, consistent with causality. They are represented by the internal potential ψ, yielding the velocity $\boldsymbol{u} = (N^2 \nabla_h - \omega^2 \nabla)\psi$, with $\nabla = (\partial/\partial x, \partial/\partial y, \partial/\partial z)$ the del operator, $\nabla_h = (\partial/\partial x, \partial/\partial y, 0)$ its horizontal projection and z the upward vertical coordinate. The potential satisfies the wave equation

$$(N^2 \nabla_h^2 - \omega^2 \nabla^2)\psi = 0, \tag{3.1}$$

together with the boundary condition

$$\left(N^2 \frac{\partial}{\partial n_h} - \omega^2 \frac{\partial}{\partial n}\right)\psi = U_n \quad (\boldsymbol{x} \in S_+), \tag{3.2}$$

where $\partial/\partial n = \boldsymbol{n} \cdot \nabla$ and $\partial/\partial n_h = \boldsymbol{n} \cdot \nabla_h$.
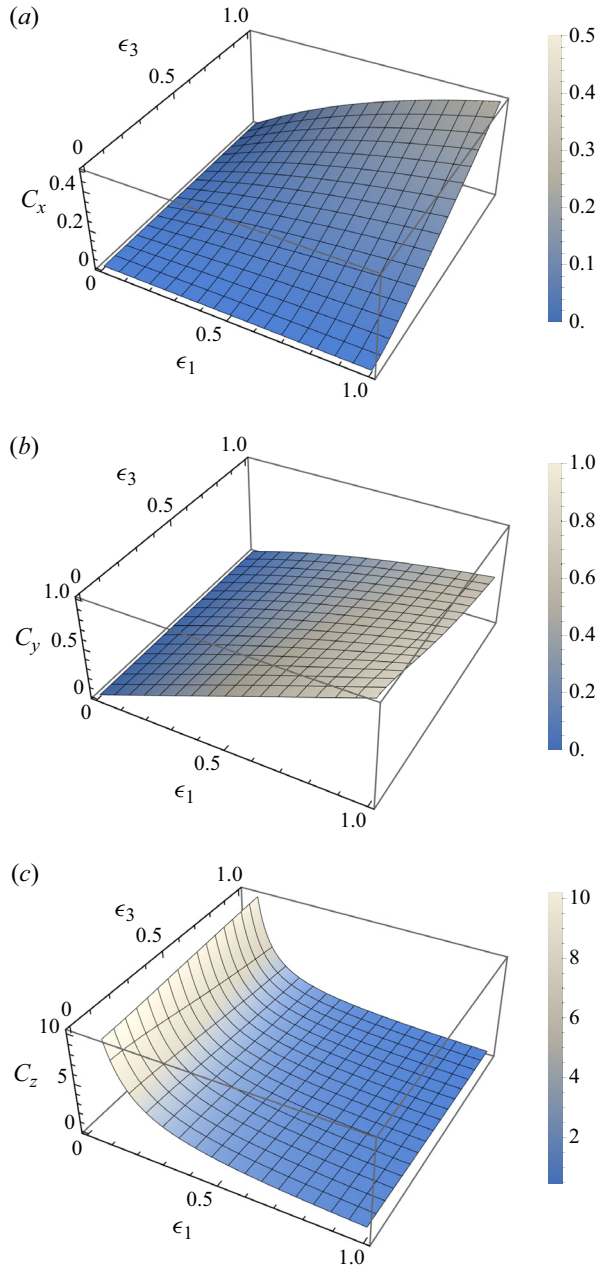
Figure 2. Added mass coefficients for the translation of an ellipsoid of semi-axes $a > b > c$ along the associated directions (*a*) x, (*b*) y and (*c*) z in a homogeneous fluid. The coefficients are determined by the aspect ratios $\epsilon_1 = c/b$ and $\epsilon_3 = b/a$.

3.1. *Representation*

The single layer (2.3) generates the potential

$$\psi(\boldsymbol{x}) = \frac{1}{4\pi(\omega^2 - N^2)^{1/2}} \int_S \frac{\sigma(\boldsymbol{x}')\,\mathrm{d}^2 S'}{[(\omega^2(\boldsymbol{x} - \boldsymbol{x}')^2 - N^2(z - z')^2]^{1/2}}, \tag{3.3}$$

999 A59-11

where the determination of the square roots is set by cuts, extending vertically downwards away from the branch points $\pm N$ and $\pm N|z - z'|/|x - x'|$ in the ω-plane. The boundary condition becomes

$$U_n(x) = \frac{1}{4\pi(\omega^2 - N^2)^{1/2}} \left(N^2 \frac{\partial}{\partial n_h} - \omega^2 \frac{\partial}{\partial n}\right)$$

$$\times \int_S \frac{\sigma(x')\, \mathrm{d}^2 S'}{[(\omega^2(x - x')^2 - N^2(z - z')^2]^{1/2}} \quad (x \in S_+). \tag{3.4}$$

We follow the approach introduced by Bryan (1889) for inertial waves, Pierce (1963) for acoustic-gravity waves and Hurley (1972) for internal waves; namely, we consider real evanescent frequencies $\omega > N$ first, stretching the coordinates anisotropically so as to transform the wave equation into the Laplace equation, then we continue the solution analytically to the upper half of the complex ω-plane.

The coordinates are stretched according to

$$x_\star = \frac{\omega}{N}x, \quad y_\star = \frac{\omega}{N}y, \quad z_\star = \left(\frac{\omega^2}{N^2} - 1\right)^{1/2} z. \tag{3.5a–c}$$

This transforms the boundary condition into

$$U_n(x) = \frac{1}{4\pi N(\omega^2 - N^2)^{1/2}} \left(N^2 \frac{\partial}{\partial n_h} - \omega^2 \frac{\partial}{\partial n}\right) \int_S \frac{\sigma(x')}{|x_\star - x'_\star|}\, \mathrm{d}^2 S' \quad (x \in S_+), \tag{3.6}$$

and the ellipsoid (2.6) into another, with semi-axes

$$a_\star = \frac{\omega}{N}a, \quad b_\star = \frac{\omega}{N}b, \quad c_\star = \left(\frac{\omega^2}{N^2} - 1\right)^{1/2} c. \tag{3.7a–c}$$

We assume that $a > b > c$, so that $a_\star > b_\star > c_\star$, and we introduce two systems of ellipsoidal coordinates: one (ρ, μ, ν) in unstretched space, with semi-axes (a, b, c) and semi-focal distances (h_1, h_2, h_3), such that $\rho = a$ on the ellipsoid; and another $(\rho_\star, \mu_\star, \nu_\star)$ in stretched space, with semi-axes $(a_\star, b_\star, c_\star)$ and semi-focal distances $(h_{1_\star}, h_{2_\star}, h_{3_\star})$, such that $\rho_\star = a_\star$ on the ellipsoid. The boundary condition becomes

$$U_n(\mu, \nu) = -\frac{b_\star c_\star}{4\pi} \frac{\partial}{\partial \rho_\star} \int_{\rho'=a} \frac{\sigma(\mu', \nu')}{|x_\star - x'_\star|} \frac{(a^2 - \mu'^2)^{1/2}(a^2 - \nu'^2)^{1/2}}{(a^2 - \mu^2)^{1/2}(a^2 - \nu^2)^{1/2}}\, \mathrm{d}\varpi' \quad (\rho = a + 0). \tag{3.8}$$

The difficulty lies in the fact that differentiation is performed in stretched coordinates, while integration is performed in unstretched coordinates.

However, even though the coordinates (μ, ν) and $(\mu_\star, \nu_\star)$ are distinct on the ellipsoid, the eccentric angles (ϑ, φ) are not, since

$$\frac{x}{a} = \frac{x_\star}{a_\star} = \cos\vartheta, \quad \frac{y}{b} = \frac{y_\star}{b_\star} = \sin\vartheta \cos\varphi, \quad \frac{z}{c} = \frac{z_\star}{c_\star} = \sin\vartheta \sin\varphi, \tag{3.9a–c}$$

with two consequences. First, the boundary condition becomes

$$U_n(\mu, \nu) = -\frac{b_\star c_\star}{4\pi} \frac{\partial}{\partial \rho_\star} \int_0^{2\pi} \int_0^\pi \frac{\sigma(\mu', \nu')}{|x_\star - x'_\star|} \frac{(a^2 - \mu'^2)^{1/2}(a^2 - \nu'^2)^{1/2}}{(a^2 - \mu^2)^{1/2}(a^2 - \nu^2)^{1/2}} \sin\vartheta'\, \mathrm{d}\vartheta'\, \mathrm{d}\varphi', \tag{3.10}$$

where $\rho'_\star = a_\star$ and $\rho_\star = a_\star + 0$. Second, the same surface harmonics $s_l^m(\vartheta, \varphi)$ are involved, on the one hand in the expansions (2.10) and (2.11) of $U_n(\mu, \nu)$ and $\sigma(\mu, \nu)$,

999 A59-12

respectively, and on the other hand in the expansion of $1/|\boldsymbol{x}_\star - \boldsymbol{x}'_\star|$, yielding, for $\rho'_\star = a_\star$ and $\rho_\star = a_\star + 0$,

$$
\frac{\partial}{\partial \rho_\star} \frac{1}{|\boldsymbol{x}_\star - \boldsymbol{x}'_\star|} = -\frac{4\pi}{b_\star c_\star} \sum_{l=0}^{\infty} \sum_{m=1}^{2l+1} [1 - b_\star c_\star E_l^m(a_\star) E_l^{m\,\prime}(a_\star) I_l^m(a_\star)] s_l^m(\vartheta, \varphi) s_l^m(\vartheta', \varphi').
$$
(3.11)

Accordingly, the only change in the results of §§ 2.1 and 2.2 is the replacement of a, b and c by $a_\star$, $b_\star$ and $c_\star$ in the relation between σ_{lm} and U_{lm}, consistent with the rule of affine similitude put forward by Ermanyuk (2002). We obtain

$$
\sigma_{lm} = \frac{U_{lm}}{1 - b_\star c_\star E_l^m(a_\star) E_l^{m\,\prime}(a_\star) I_l^m(a_\star)}.
$$
(3.12)

Analytic continuation to the upper half of the ω-plane allows the extension of this solution to other values of ω and other orderings of a, b and c.

3.2. *Dipolar oscillations*

Monopolar oscillations are unaffected by the stratification, but dipolar oscillations are. The relevant geometrical parameters are the horizontal aspect ratio $\epsilon_h = b/a$ and the vertical aspect ratio $\epsilon_v = c/b$, and the relevant physical parameter is the frequency ratio $\Omega = \omega/N$. We introduce

$$
\Upsilon_v = \frac{c_\star}{b_\star} = \epsilon_v \left(1 - \frac{1}{\Omega^2}\right)^{1/2},
$$
(3.13)

generalizing the notation Υ of Voisin (2021, 2024). Equations (2.33)–(2.35) for the equivalent source and dipole strength remain valid, with

$$
A(\Upsilon_v, \epsilon_h) = \frac{\epsilon_h^2 \Upsilon_v}{1 - \epsilon_h^2} \frac{F(\alpha, \beta) - E(\alpha, \beta)}{(1 - \epsilon_h^2 \Upsilon_v^2)^{1/2}},
$$
(3.14a)

$$
B(\Upsilon_v, \epsilon_h) = \frac{\epsilon_h^2 \Upsilon_v}{1 - \epsilon_h^2} \frac{E(\alpha, \beta)/(1 - \beta) - F(\alpha, \beta)}{(1 - \epsilon_h^2 \Upsilon_v^2)^{1/2}} - \frac{\Upsilon_v^2}{1 - \Upsilon_v^2},
$$
(3.14b)

$$
C(\Upsilon_v, \epsilon_h) = \frac{1}{1 - \Upsilon_v^2} - \frac{\Upsilon_v}{1 - \Upsilon_v^2} \frac{E(\alpha, \beta)}{(1 - \epsilon_h^2 \Upsilon_v^2)^{1/2}},
$$
(3.14c)

where

$$
\alpha = \arccos(\epsilon_h \Upsilon_v), \quad \beta = \frac{1 - \epsilon_h^2}{1 - \epsilon_h^2 \Upsilon_v^2}.
$$
(3.15a,b)

The limit $\epsilon_h \to 1$ corresponds to a spheroid of vertical z-axis and gives

$$
A = B = \frac{1 - D(\Upsilon_v)}{2}, \quad C = D(\Upsilon_v) = \frac{1}{1 - \Upsilon_v^2} \left[1 - \frac{\Upsilon_v \arccos \Upsilon_v}{(1 - \Upsilon_v^2)^{1/2}}\right],
$$
(3.16a,b)

while the limit $\epsilon_h \to 0$ corresponds to an elliptic cylinder of horizontal x-axis and gives

$$
A = 0, \quad B = \frac{\Upsilon_v}{1 + \Upsilon_v}, \quad C = \frac{1}{1 + \Upsilon_v}.
$$
(3.17a–c)

Both limits are consistent with Voisin (2021, 2024).

3.3. *Added mass*

In the presence of density stratification, the added mass coefficients vary with the frequency. For a body having the horizontal x- and y-axes and the vertical z-axis as principal directions, the coefficients have been shown by Ermanyuk ([2002](#)) and Voisin ([2024](#)) to be

$$C_x(\omega) = \frac{\mathcal{D}_x}{\mathcal{V}U} - 1, \quad C_y(\omega) = \frac{\mathcal{D}_y}{\mathcal{V}V} - 1, \quad C_z(\omega) = \left(1 - \frac{N^2}{\omega^2}\right)\left(\frac{\mathcal{D}_z}{\mathcal{V}W} - 1\right),$$

$$(3.18a\text{--}c)$$

yielding for the ellipsoid

$$C_x(\omega) = \frac{A}{1-A}, \quad C_y(\omega) = \frac{B}{1-B}, \quad C_z(\omega) = \left(1 - \frac{1}{\Omega^2}\right)\frac{C}{1-C}. \qquad (3.19a\text{--}c)$$

The variations of these coefficients are plotted in [figures 3–5](#), for several values of ϵ_h and ϵ_v between 1/5 and 5. The same trends are observed as for the spheroid of Voisin ([2024](#)), corresponding to $\epsilon_h = 1$. For the inertial coefficients, finite values ϵ_h of $\mathrm{Re}\, C_x(\omega)$ and $1/\epsilon_h$ of $\mathrm{Re}\, C_y(\omega)$ are obtained at $\Omega = 0$, and a logarithmic divergence of $\mathrm{Re}\, C_z(\omega)$. The coefficients are zero at $\Omega = 1$, then they increase towards their values C_x^∞, C_y^∞ and C_z^∞ in the absence of stratification, reached for $\Omega \to \infty$. The damping coefficients $\Omega\, \mathrm{Im}\, C_x(\omega)$, $\Omega\, \mathrm{Im}\, C_y(\omega)$ and $\Omega\, \mathrm{Im}\, C_z(\omega)$ are zero not only at $\Omega = 0$ and 1, but also for all the frequencies $\Omega > 1$ at which the waves are evanescent.

A transition is observed, as ϵ_h decreases down to 0, from the three-dimensional ellipsoid to the two-dimensional elliptic cylinder. As $\epsilon_h \to 0$, all three added mass coefficients, once normalized by their values in the absence of stratification, have the same limiting behaviour

$$\frac{C_x(\omega)}{C_x^\infty} = \frac{C_y(\omega)}{C_y^\infty} = \frac{C_z(\omega)}{C_z^\infty} = \left(1 - \frac{1}{\Omega^2}\right)^{1/2}, \qquad (3.20)$$

with $C_x^\infty = 0$, $C_y^\infty = \epsilon_v$ and $C_z^\infty = 1/\epsilon_v$. This behaviour is characterized not only by the absence of wave damping at the evanescent frequencies $\Omega > 1$, but also by the absence of inertial effects at the propagating frequencies $\Omega < 1$. The transition is shown in [figures 6–8](#) for several values of ϵ_h between 0 and 10. The normalized coefficients undergo little change as ϵ_h increases above 1.

4. Applications

The implications of these results are now discussed for the force exerted on a moving body, and the wave energy radiated away from an oscillating body. The body is assumed to have the x-, y- and z-axes as principal directions, and to displace a mass $m_f = \rho_0 \mathcal{V}$ of fluid, with ρ_0 the fluid density and $\mathcal{V}$ the body volume.

4.1. *Impulse response function*

When the body moves at the velocity $\boldsymbol{U}(t) = U(t)\boldsymbol{e}_x + V(t)\boldsymbol{e}_y + W(t)\boldsymbol{e}_z$, the fluid exerts on it a hydrodynamic force of x-component

$$F_x(t) = -m_f C_x^\infty \frac{\mathrm{d}U}{\mathrm{d}t}(t) - m_f N \int_0^\infty C_x^M(t') \frac{\mathrm{d}U}{\mathrm{d}t}(t - t')\, \mathrm{d}t', \qquad (4.1)$$
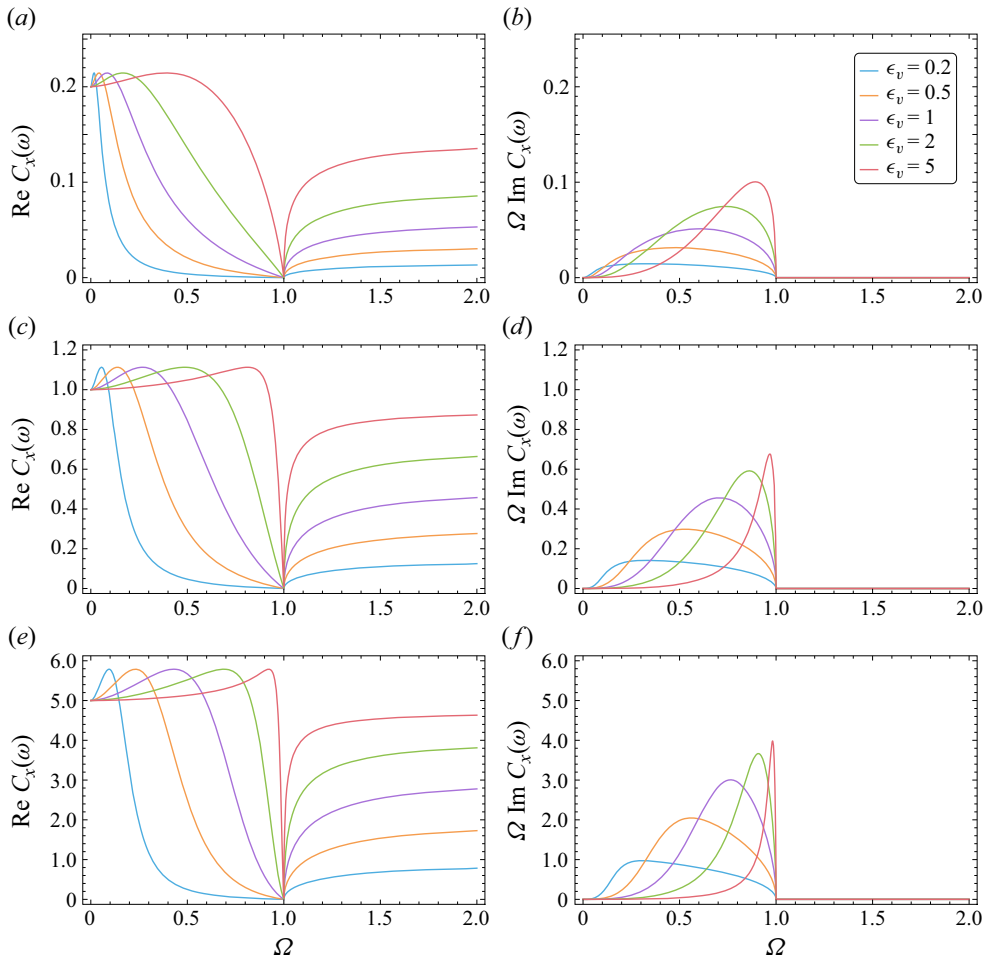
Figure 3. Frequency variations of (a,c,e) the inertial coefficient $\mathrm{Re}\, C_x(\omega)$ and (b,d,f) the damping coefficient $\Omega\,\mathrm{Im}\, C_x(\omega)$ of an ellipsoid of horizontal aspect ratio ϵ_h and vertical aspect ratio ϵ_v, oscillating along the horizontal x-axis in a stratified fluid, for (a,b) $\epsilon_h = 0.2$, (c,d) $\epsilon_h = 1$ and (e,f) $\epsilon_h = 5$.

and similarly for the y- and z-components, with

$$C_x^M(t) = \frac{1}{2\pi N} \int [C_x(\omega) - C_x^\infty] \exp(-\mathrm{i}\omega t)\, \mathrm{d}\omega \tag{4.2}$$

the impulse response function (Cummins 1962; Ogilvie 1964). Accordingly, the force acting on the body combines the same acceleration reaction as in a homogeneous fluid, plus a memory integral representing, in the stratified fluid, the effect of internal wave radiation. As stated by Newman (2017, § 6.19) for surface gravity waves, when the body moves, 'waves will be generated [...]. As time increases, these waves will propagate outward from the body, but they will continue to affect the fluid pressure and hence the body force for all subsequent times. Thus *memory effects* are introduced.'
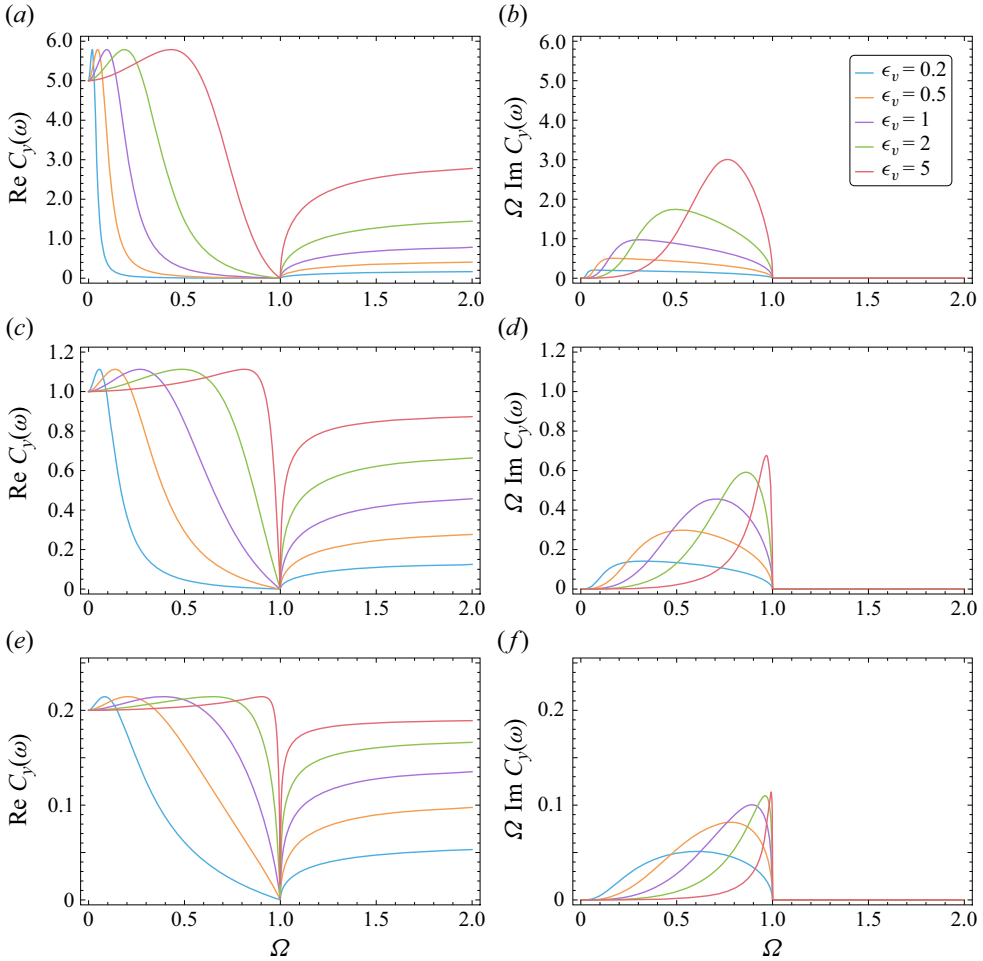
Figure 4. Same as figure 3 for oscillations along the horizontal y-axis.

Owing to causality, and to the Hermitian property $C_x(-\omega) = \overline{C_x(\omega)}$, where the overbar denotes a complex conjugate, the impulse response function may be written as

$$C_x^M(t) = \frac{2}{\pi} \frac{H(t)}{N} \int_0^N \text{Im}[C_x(\omega)] \sin(\omega t) \, d\omega, \tag{4.3}$$

with $H(t)$ the Heaviside step function, and the integral evaluated numerically as, say,

$$C_x^M(t) = \frac{2}{\pi} H(t) \int_0^{\pi/2} \text{Im}[C_x(N \cos\theta)] \sin(Nt \cos\theta) \sin\theta \, d\theta. \tag{4.4}$$

The same applies to $C_y^M(t)$ and $C_z^M(t)$. The variations of these functions are presented in figure 9, normalized by C_x^∞, C_y^∞ and C_z^∞, with time normalized by the buoyancy period $T = 2\pi/N$. As for added mass in figures 6–8, a transition is observed, as $\epsilon_h \to 0$, to the response for the elliptic cylinder, identical in all directions and given by

$$\frac{C_x^M(t)}{C_x^\infty} = \frac{C_y^M(t)}{C_y^\infty} = \frac{C_z^M(t)}{C_z^\infty} = H(t) \int_0^t J_1(N\tau) \frac{d\tau}{\tau}, \tag{4.5}$$

999 A59-16
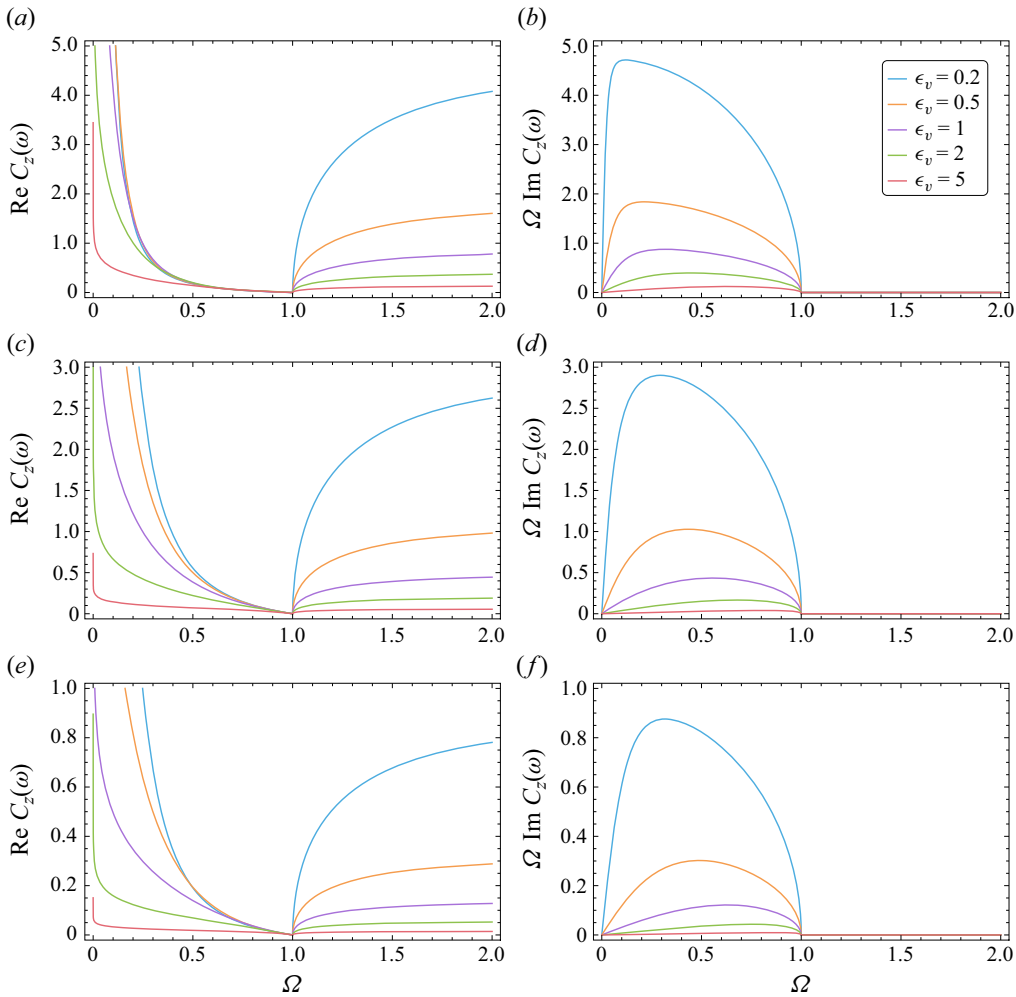
Figure 5. Same as figure 3 for oscillations along the vertical *z*-axis.

where

$$\int_0^t J_1(N\tau) \frac{d\tau}{\tau} = Nt\, J_0(Nt)\left[1 - \frac{\pi}{2}\boldsymbol{H}_1(Nt)\right] - J_1(Nt)\left[1 - \frac{\pi}{2}Nt\boldsymbol{H}_0(Nt)\right], \qquad (4.6)$$

with J_n a Bessel function and $\boldsymbol{H}_n$ a Struve function.

The properties already observed for the spheroid of Voisin (2024) are confirmed. The impulse response function is positive for vertical motion, implying that the memory force always opposes the vertical acceleration of the body, consistent with the inhibition of vertical motions by the stratification. For horizontal motion, the response function is alternatively positive and negative, meaning that the force alternatively opposes and fosters horizontal acceleration.

The response function starts from 0 at $t = 0$, increases steadily to a maximum after approximately half a buoyancy period, then decreases slowly for vertical motion and faster for horizontal motion, while also performing decaying oscillations at the buoyancy frequency. For horizontal motion, the decrease vanishes above a threshold value of ϵ_v. For the spheroid, the asymptotics of Voisin (2024) showed the threshold to be $\epsilon_v = 2.40$,
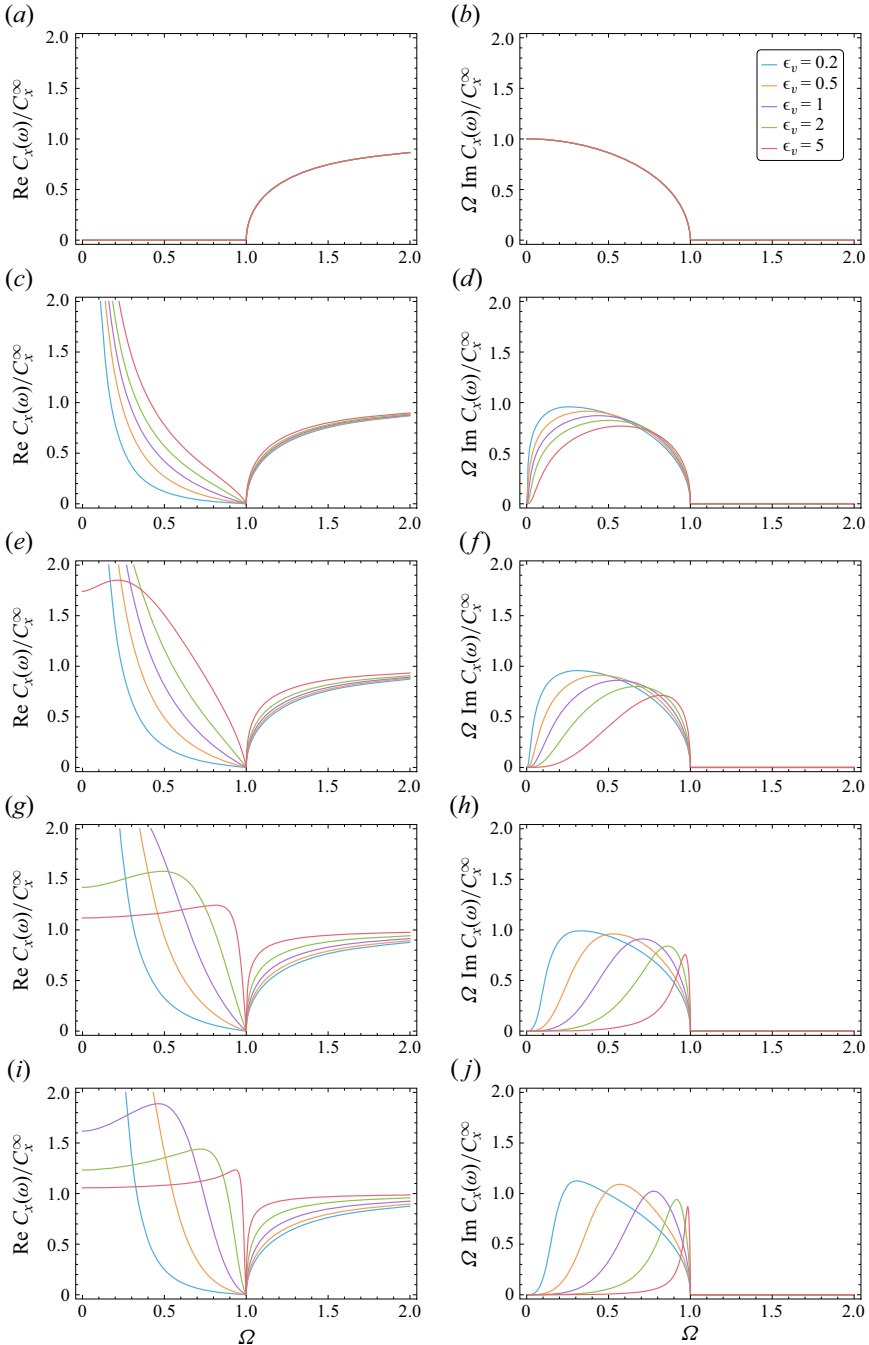
Figure 6. Transition to two-dimensionality for (a,c,e,g,i) the inertial coefficients and (b,d,f,h,j) the damping coefficients as ϵ_h decreases down to 0 for oscillations along the x-axis, and (a,b) $\epsilon_h = 0$, (c,d) $\epsilon_h = 0.01$, (e,f) $\epsilon_h = 0.1$, (g,h) $\epsilon_h = 1$ and (i,j) $\epsilon_h = 10$.
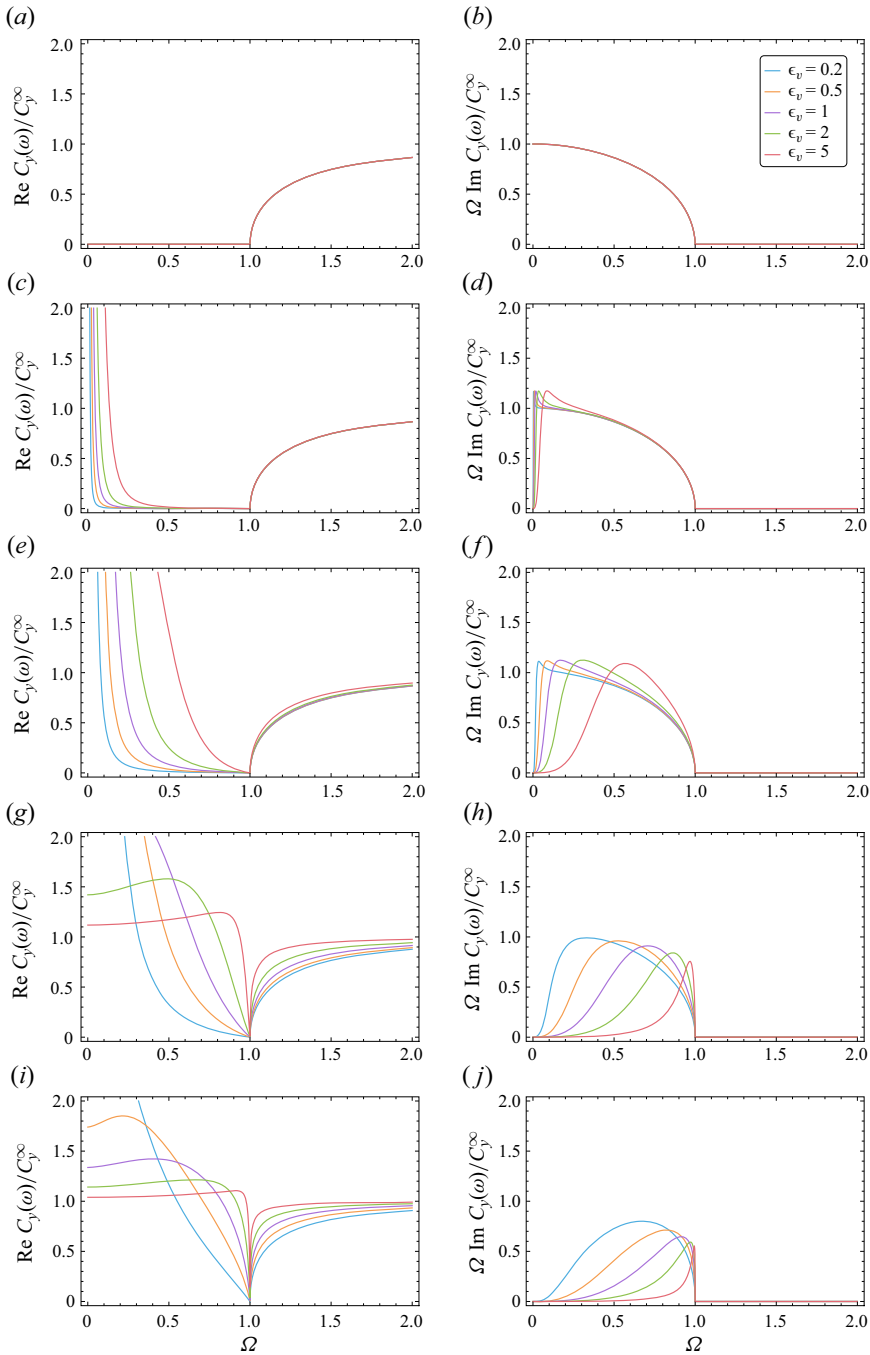
Figure 7. Same as figure 6 for oscillations along the *y*-axis.

and the decrease to be algebraic and as t^{-1} for vertical motion, exponential for horizontal motion and the buoyancy oscillations to decay as $t^{-3/2}$. Accordingly, the memory effect is delayed by half a buoyancy period and operates over a smaller time range than that, as
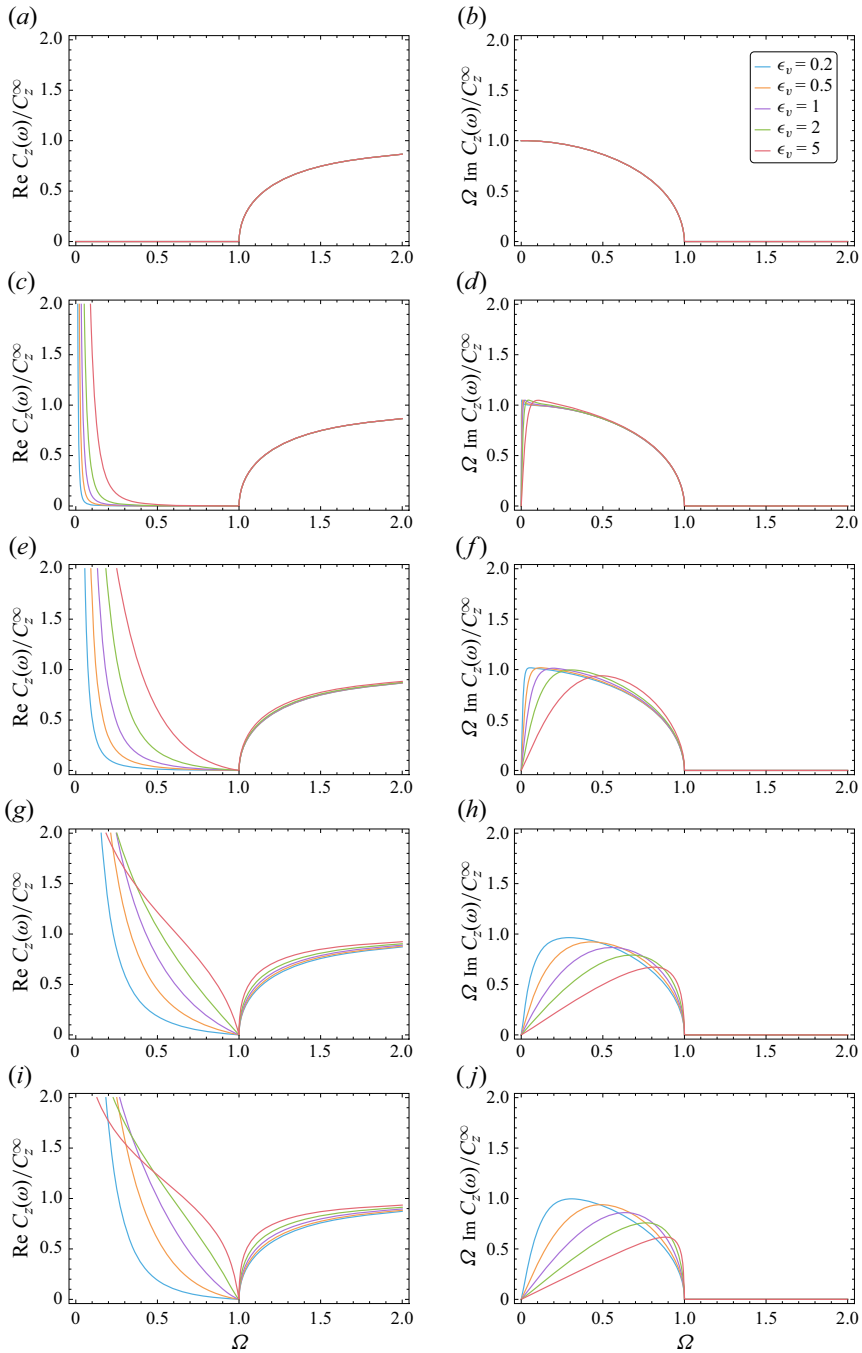
Figure 8. Same as figure 6 for oscillations along the *z*-axis.

$t^{-1/2}$, associated with the Basset–Boussinesq force and caused by viscous boundary-layer dissipation in a homogeneous fluid.

The situation changes as ϵ_h gets smaller and the ellipsoid transitions to an elliptic cylinder. In that event, the decrease of the response function slows down until eventually,

999 A59-20
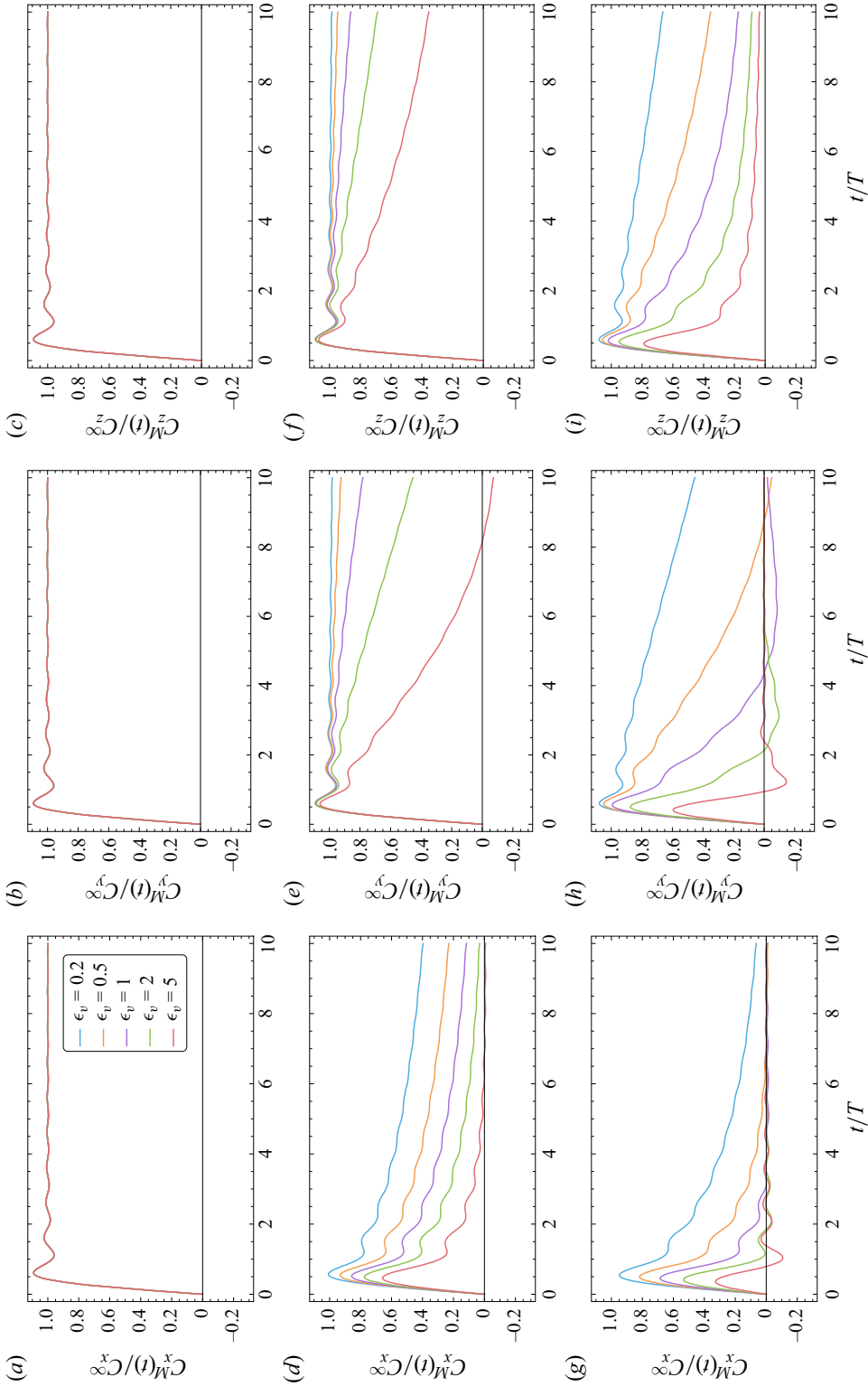
Figure 9. For caption see next page.
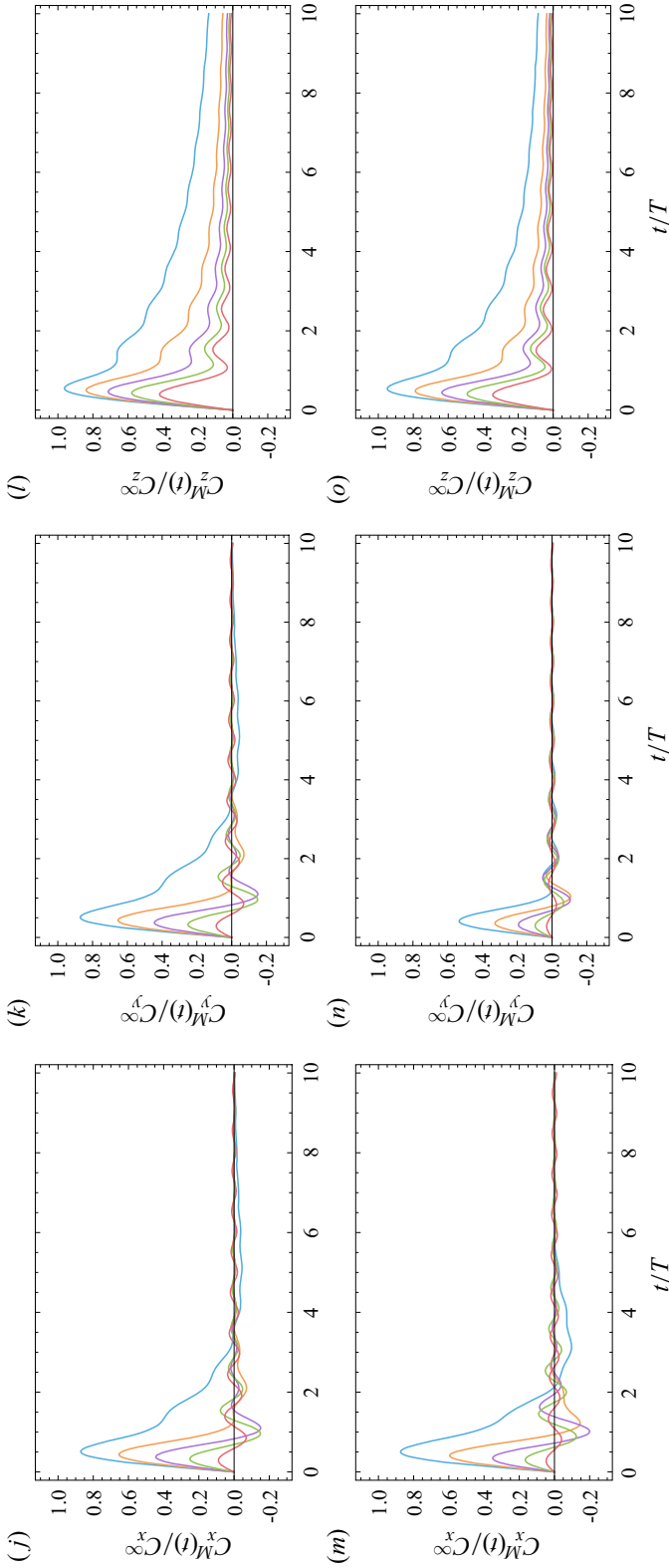
Figure 9. Impulse response functions of an ellipsoid of horizontal aspect ratio $(a-c)$ $\epsilon_h = 0$, $(d-f)$ $\epsilon_h = 0.01$, $(g-i)$ $\epsilon_h = 0.1$, $(j-l)$ $\epsilon_h = 1$ or $(m-o)$ $\epsilon_h = 10$, and vertical aspect ratio ϵ_v, for motions along (a,d,g,j,m) the x-axis, (b,e,h,k,n) the y-axis and (c,f,i,l,o) the z-axis.

for $\epsilon_h = 0$, the response function (4.5) of the cylinder is obtained, identical for all directions of motion, always positive and tending to 1 as $Nt \to \infty$. When this happens, the whole past history of the cylinder affects equally the reaction of the fluid at any subsequent time, and this reaction always opposes the acceleration of the cylinder.

4.2. *Energy radiation*

When the body oscillates at the velocity $U \exp(-i\omega t)$, with $U = U\boldsymbol{e}_x + V\boldsymbol{e}_y + W\boldsymbol{e}_z$, and U, V and W real, the waves radiated in the fluid carry away the average power

$$P = \tfrac{1}{2} m_f \omega \{U^2 \operatorname{Im}[C_x] + V^2 \operatorname{Im}[C_y] + W^2 \operatorname{Im}[C_z]\}, \tag{4.7}$$

becoming, for the ellipsoid of volume $\mathcal{V} = (4/3)\pi abc$,

$$P = \frac{2}{3}\pi\rho_0 N\Omega abc \left\{ U^2 \operatorname{Im}\left[\frac{A}{1-A}\right] + V^2 \operatorname{Im}\left[\frac{B}{1-B}\right] + \left(1 - \frac{1}{\Omega^2}\right) W^2 \operatorname{Im}\left[\frac{C}{1-C}\right] \right\}, \tag{4.8}$$

with A, B and C given in (3.14).

The variations of this power with Ω at fixed excursion $\mathcal{A} = |U|/(N\Omega)$ are represented in figure 10, normalized by $P_0 = \rho_0 \mathcal{V} N^3 \mathcal{A}^2$, separately for the three directions of oscillation, for aspect ratios ϵ_h and ϵ_v between $1/5$ and 5. The same general shape is observed in all cases, similar to that reported by Voisin (2024) for the spheroid, namely zero energy radiation at $\Omega = 0$ and $\Omega \geqslant 1$, and in between a single maximum at a frequency ratio Ω_m. The variations of Ω_m are plotted in figure 11 for ϵ_h and ϵ_v between 10^{-2} and 10^2, yielding values between 0.78 and 1, the lower values being reached when ϵ_v is small, and the higher values when ϵ_h and ϵ_v are moderate or large.

5. Conversion rate

Conversion rate is the name given to the average wave power when the waves are generated by barotropic tidal oscillations over topography at the bottom of the stratified ocean. Three investigations will be our focus in the following: the analytical work by Llewellyn Smith & Young (2002), based on the weak-topography approximation, and the numerical works by Holloway & Merrifield (1999) and Munroe & Lamb (2005), using the Princeton ocean model. In these, the barotropic tide has an elliptic polarization, instead of the present linear polarization; the hydrostatic approximation is made, namely the tidal frequency is assumed small compared with the buoyancy frequency, so that the vertical acceleration of the fluid is neglected; the ocean is rotating, so that the waves are affected by the Coriolis force; the depth is finite and the buoyancy frequency varies vertically, so that the waves decompose into vertical modes. All these differences are of secondary importance for the aspects considered here; we will come back to them later in § 6. Accordingly, we investigate the oscillatory flow at the velocity $(U\boldsymbol{e}_x + V\boldsymbol{e}_y) \exp(-i\omega t)$, with U and V real, over topography $h(x, y)$ at the bottom $z = 0$ of a semi-infinite non-rotating uniformly stratified fluid of buoyancy frequency N. The tidal frequency is assumed to satisfy $\omega < N$, so that the waves propagate at the angle $\arccos(\omega/N)$ to the vertical.
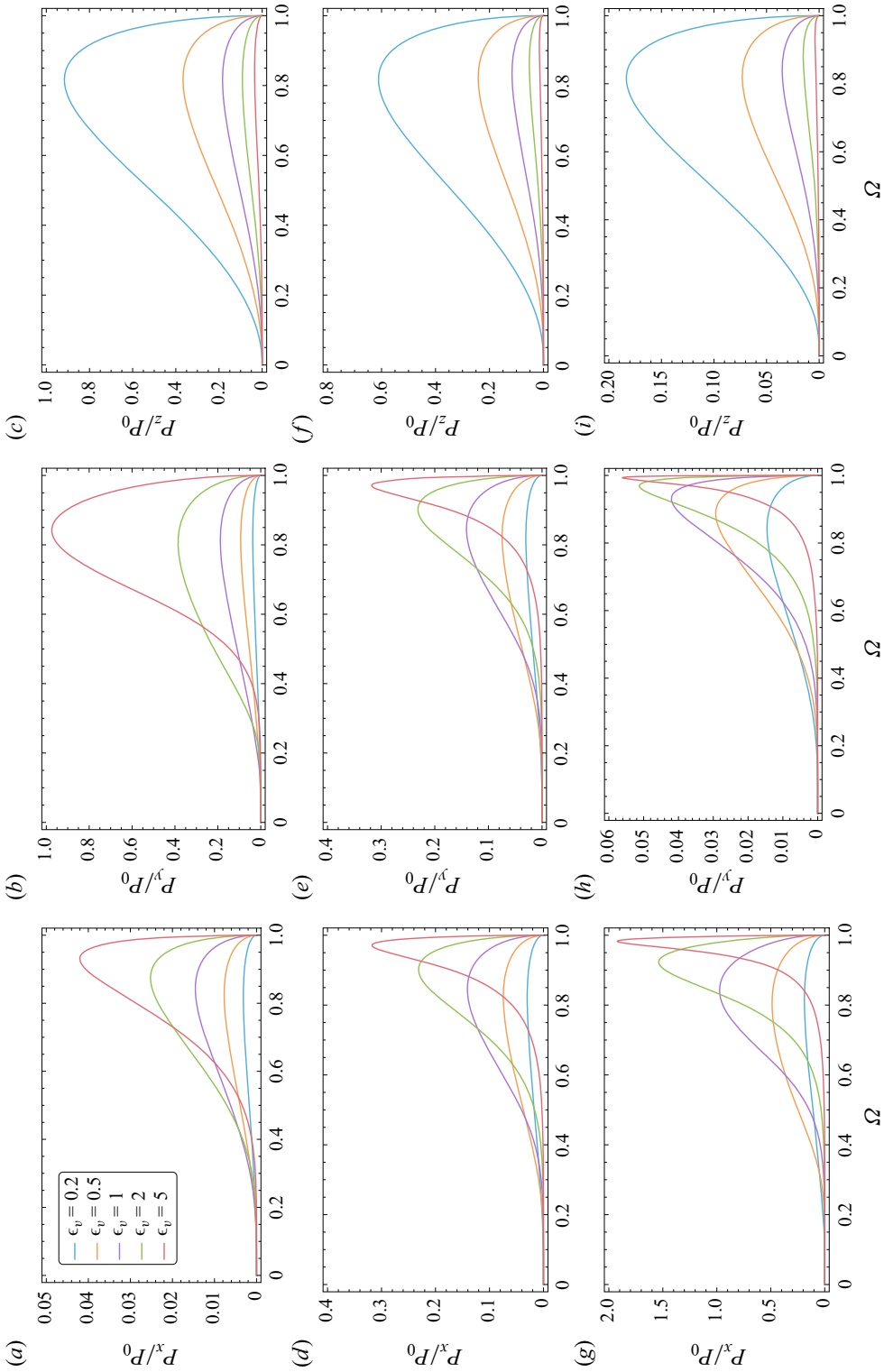
Figure 10. Radiated wave power for the oscillations of an ellipsoid of horizontal aspect ratio $(a–c)$ $\epsilon_h = 0.2$, $(d–f)$ $\epsilon_h = 1$ or $(g–i)$ $\epsilon_h = 5$, and vertical aspect ratio ϵ_v, along (a,d,g) the x-axis, (b,e,h) the y-axis and (c,f,i) the z-axis. The amplitude of the oscillations is kept constant.
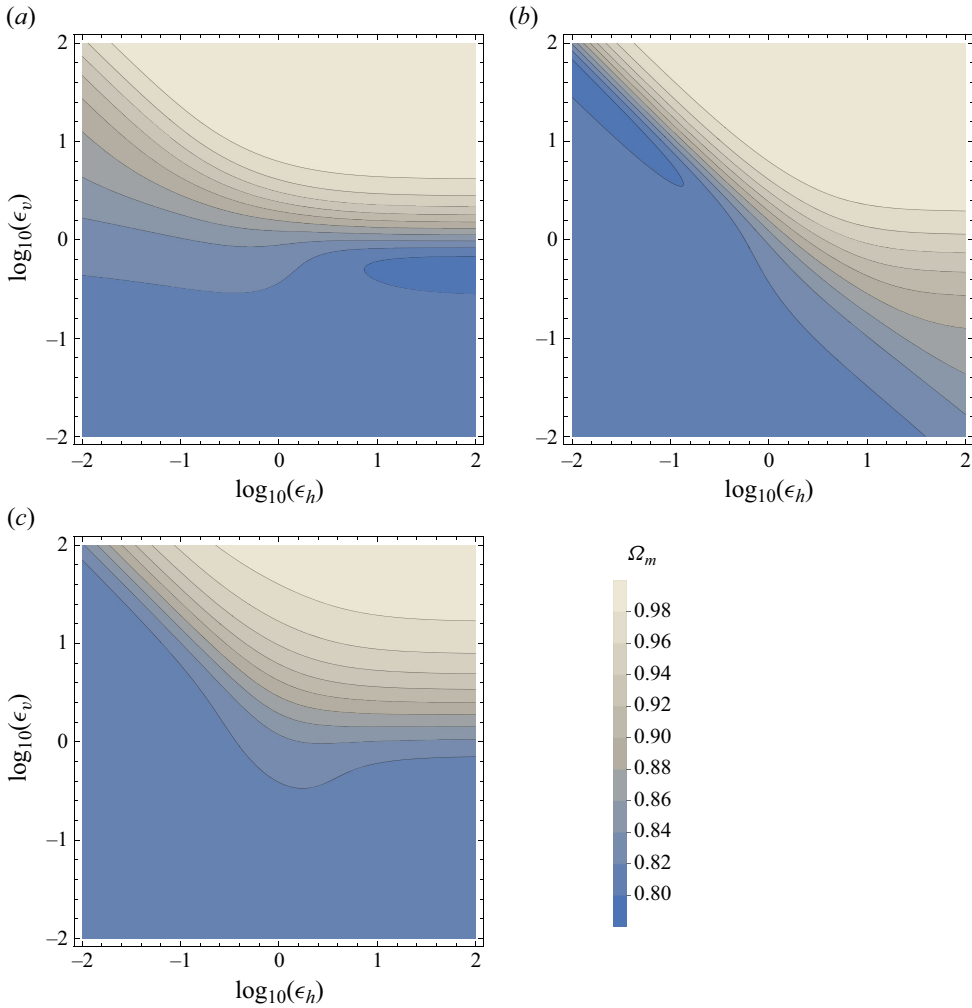
Figure 11. Frequency of maximum energy radiation for oscillations along (*a*) the *x*-axis, (*b*) the *y*-axis and (*c*) the *z*-axis.

5.1. *Conversion by ridges*

In two dimensions, namely for a ridge along the *y*-axis, with cross-section $h(x)$ and spectrum

$$h(k_x) = \int h(x) \exp(-\mathrm{i}k_x x) \, \mathrm{d}x, \tag{5.1}$$

the weak-topography approximation (WTA) assumes that the steepness ratio

$$\gamma = \max |h'(x)| \left(\frac{N^2}{\omega^2} - 1 \right)^{1/2}, \tag{5.2}$$

comparing the topographic slope to the slope of the wave rays (Balmforth *et al.* 2002; Balmforth & Peacock 2009), is small. The conversion rate follows, per unit length in the

Topography	$h(x)$	$h(k_x)$	P
Gaussian	$c \exp\left(-\dfrac{x^2}{2a^2}\right)$	$(2\pi)^{1/2}ac\exp\left(-\dfrac{k_x^2 a^2}{2}\right)$	$\dfrac{1}{2}\rho_0(N^2-\omega^2)^{1/2}c^2 U^2$
Ellipse	$c\left(1-\dfrac{x^2}{a^2}\right)^{1/2}$	$\pi c \dfrac{J_1(k_x a)}{k_x}$	$\dfrac{\pi}{4}\rho_0(N^2-\omega^2)^{1/2}c^2 U^2$

Table 1. Conversion rates of two-dimensional ridges.

y-direction, as

$$P = \frac{\rho_0(N^2-\omega^2)^{1/2}U^2}{4\pi}\int |k_y|\,|h(k_y)|^2\,\mathrm{d}k_y. \tag{5.3}$$

See for example Bühler & Muller (2007).

The rates for Gaussian and elliptic ridges of height c and width a are given in table 1. For the Gaussian ridge, the WTA has been used. For the elliptic ridge, identical results are obtained using the WTA, or complementing the ridge with its image through the bottom (to account for the waves emitted downwards then reflected at the bottom), applying the limit (3.17) to (4.8), interchanging the x- and y-axes, dividing the outcome by the volume of the ellipsoid, multiplying it by the cross-section of the cylinder, then taking half the result (to account for wave radiation in the half-space $z > 0$).

The variation of the conversion rates as c^2 is consistent with (5.3), as is their independence of a: Bühler & Muller (2007) pointed out that one consequence of (5.3) is the invariance of the conversion upon horizontal stretching of the topography. Accordingly, the same rate is obtained here for the elliptic ridge, as for the vertical knife edge of Llewellyn Smith & Young (2003) and the circular ridge of Voisin *et al.* (2011). All this hints at an applicability of the WTA far beyond its expected range of validity, at least in two dimensions.

5.2. *Conversion by seamounts*

In three dimensions, for a seamount $h(x, y)$ of spectrum (1.2), the steepness ratio becomes

$$\gamma = \max|\nabla h(x, y)|\left(\frac{N^2}{\omega^2} - 1\right)^{1/2}, \tag{5.4}$$

and the WTA conversion rate is given by (1.1). Bühler & Muller (2007) deduced from it an invariance of the conversion, upon shrinking the topography horizontally by a given factor, provided the topography is also stretched vertically by the square root of this factor.

The conversion rates for Gaussian and ellipsoidal seamounts of height c, and horizontal radii a and b are given in table 2. Following Llewellyn Smith & Young (2002), they have been separated into two factors: one, P_{axi}, representing the effect of an axisymmetric seamount of equivalent radius $d = (ab)^{1/2}$; and the other, P/P_{axi}, representing the effect of asymmetry, with $\epsilon'_h = a/b$ the horizontal aspect ratio and χ the angle of the barotropic velocity (U, V) to the x-axis. Also relevant for the ellipsoid are the vertical aspect ratio $\epsilon'_v = c/d$ and the quotient

$$\Upsilon'_v = \epsilon'_v\left(\frac{1}{\Omega^2} - 1\right)^{1/2} \tag{5.5}$$

Topography	$h(x,y)$	$h(k_x,k_y)$	P_{axi}	P/P_{axi}
Gaussian	$c\exp\left(-\dfrac{x^2}{2a^2}-\dfrac{y^2}{2b^2}\right)$	$2\pi abc\exp\left(-\dfrac{k_x^2a^2}{2}-\dfrac{k_y^2b^2}{2}\right)$	$\dfrac{\pi^{3/2}}{8}\rho_0(N^2-\omega^2)^{1/2}dc^2(U^2+V^2)$	$\dfrac{2}{\pi\epsilon_h'^{1/2}}\left\{E(1-\epsilon_h'^2)+\cos(2\chi)\left[\dfrac{1+\epsilon_h'^2}{1-\epsilon_h'^2}E(1-\epsilon_h'^2)\right.\right.$ $\left.\left.-\dfrac{2\epsilon_h'^2}{1-\epsilon_h'^2}K(1-\epsilon_h'^2)\right]\right\}\quad(\epsilon_h'<1)$
Ellipsoid (WTA)	$c\left(1-\dfrac{x^2}{a^2}-\dfrac{y^2}{b^2}\right)^{1/2}$	$2\pi abc\,\dfrac{j_1[(k_x^2a^2+k_y^2b^2)^{1/2}]}{(k_x^2a^2+k_y^2b^2)^{1/2}}$	$\dfrac{\pi^2}{12}\rho_0(N^2-\omega^2)^{1/2}dc^2(U^2+V^2)$	Same as above
Ellipsoid (exact)	$c\left(1-\dfrac{x^2}{a^2}-\dfrac{y^2}{b^2}\right)^{1/2}$		$\dfrac{\pi^2}{3}\dfrac{\rho_0(N^2-\omega^2)^{1/2}dc^2(U^2+V^2)}{(1+\Upsilon_v'^2)^{3/2}|1+D(i\Upsilon_v')|^2}$	$\dfrac{\cos^2\chi\,\mathrm{Im}\left[\dfrac{A(\Upsilon_v,\epsilon_h)}{1-A(\Upsilon_v,\epsilon_h)}\right]+\sin^2\chi\,\mathrm{Im}\left[\dfrac{B(\Upsilon_v,\epsilon_h)}{1-B(\Upsilon_v,\epsilon_h)}\right]}{\mathrm{Im}\left[\dfrac{1-D(i\Upsilon_v')}{1+D(i\Upsilon_v')}\right]}$

Table 2. Conversion rates of three-dimensional seamounts. For the Gaussian seamount, $E(\beta)$ and $K(\beta)$ are the complete Legendre integrals (A19), and the expression for $\epsilon_h'>1$ follows from changing ϵ_h' into $1/\epsilon_h'$. For the ellipsoidal seamount, $\Upsilon_v=i\Upsilon_v'\epsilon_h'^{1/2}$ and $\epsilon_h=1/\epsilon_h'$.
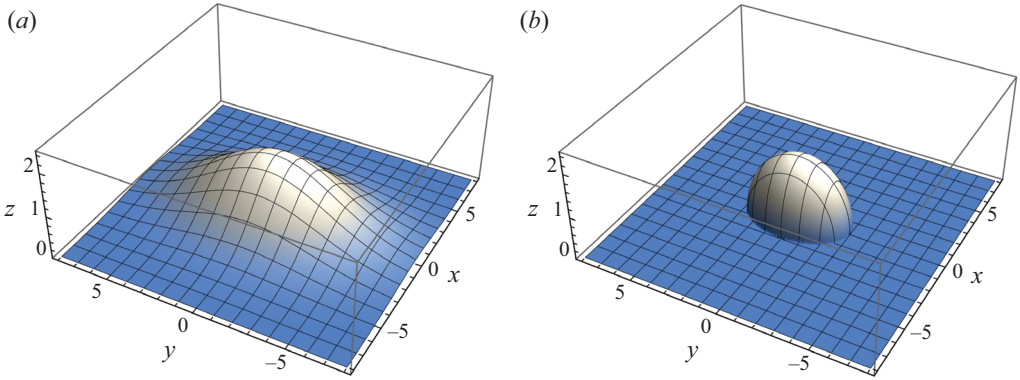
Figure 12. Equivalent (*a*) Gaussian and (*b*) ellipsoidal seamounts, having the same height and horizontal aspect ratio 2/3, and producing the same conversion in the WTA.
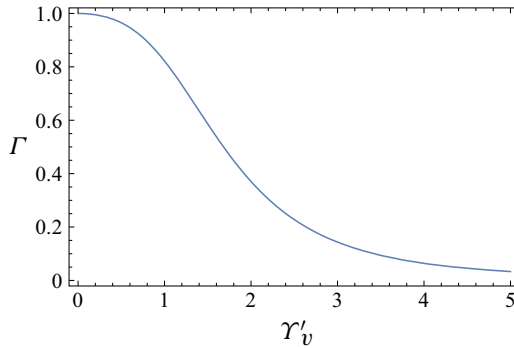

Figure 13. Ratio Γ between the conversion of a spheroidal seamount and its WTA prediction, as a function of Υ_v'.

of this ratio by the slope of the wave rays, with

$$D(\mathrm{i}\Upsilon_v') = \frac{1}{1 + \Upsilon_v'^2} \left[1 - \frac{\Upsilon_v'}{(1 + \Upsilon_v'^2)^{1/2}} \left(\mathrm{i}\frac{\pi}{2} + \operatorname{arcsinh} \Upsilon_v' \right) \right]. \tag{5.6}$$

The WTA conversion for both topographies is proportional to dc^2, consistent with the above observation by Bühler & Muller (2007). Its value for the ellipsoid differs only by a factor $2\sqrt{\pi}/3$ from that for the Gaussian. Accordingly, the conversion for a Gaussian seamount may be compared with that for an 'equivalent' ellipsoidal seamount having the same height and $3/(2\sqrt{\pi}) \approx 0.846$ times its radii. The two seamounts are shown in figure 12.

In the axisymmetric case, for the ellipsoid (in that event, a spheroid), the ratio of the exact conversion to its WTA approximation is

$$\Gamma = \frac{4}{(1 + \Upsilon_v'^2)^{3/2} |1 + D(\mathrm{i}\Upsilon_v')|^2}. \tag{5.7}$$

This ratio depends only on Υ_v', with variations plotted in figure 13. Supercriticality becomes significant for $\Upsilon_v' = 1$, say, at which point, the conversion is reduced to 82 % that for a weak topography. For $\Upsilon_v' = 2$ this percentage gets down to 37 %, and for $\Upsilon_v' = 5$ to 3 %.
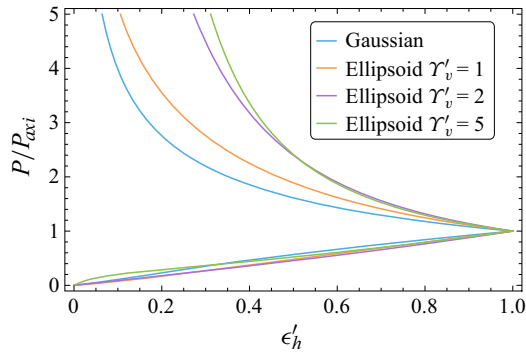
999 A59-28

Figure 14. Minimum and maximum asymmetry factors P/P_{axi} for barotropic oscillations along the major and minor axes, respectively, of a weak Gaussian seamount and ellipsoidal seamounts of $\Upsilon_v' = 1$, 2 and 5, as functions of ϵ_h'.

Llewellyn Smith & Young (2002) applied their results to a Gaussian seamount of radius $a = 16$ km and aspect ratio $\epsilon_h' = 1/3$, representative of the deep ocean around the Hawaiian islands, based on Holloway & Merrifield (1999). Taking further $c = 4000$ m, among the heights considered by Holloway & Merrifield (1999), together with $\omega = 1.4053 \times 10^{-4}$ s^{-1}, corresponding to the M_2-tide, and $N = 1.75 \times 10^{-3}$ s^{-1}, corresponding to one cycle per hour, based on figure 2(*c*) of Holloway & Merrifield (1999), we obtain $\Upsilon_v' = 2.1$, and hence $\Gamma = 0.33$, for the equivalent ellipsoidal seamount. So supercriticality reduces the conversion to one-third its WTA prediction.

The effects of asymmetry in the WTA are the same for Gaussian and ellipsoidal seamounts. They were analysed in figures 6 and 7 of Llewellyn Smith & Young (2002). At $\epsilon_h' < 1$, P/P_{axi} was seen to increase monotonically from its value for $\chi = \pi/2$, when the barotropic oscillation was along the major axis of the topography, to its value for $\chi = 0$, when the oscillation was along the minor axis. The gap between these values increased as ϵ_h' decreased, namely as the topography became more two-dimensional. For the above seamount, the lower value was 0.39 and the upper value 2.07.

The present figures 14 and 15, modelled after those, show that the same effects remain present for supercritical topography and get amplified as Υ_v' increases, namely as the ellipsoid gets steeper and the wave rays flatter. The amplification is especially visible in figure 15(*d*), together with the shrinking of the region of parameter space in which the conversion is diminished by the asymmetry. For the 'equivalent' ellipsoid, the lower value of P/P_{axi} is 0.30 and the upper value 4.09.

Munroe & Lamb (2005) investigated numerically the departures from the WTA as the seamounts become supercritical. Their figures 9 and 10 presented the evolution of the conversion rate for a Gaussian seamount of minor radius $a = 4.56$ km and horizontal aspect ratio between $\epsilon_h' = 0.1$ and 1, by steps of 0.1, as the height c of the seamount varied between 300 and 3000 m. The barotropic tide had the frequency $\omega = 1.4053 \times 10^{-4}$ s^{-1}, the current amplitude $U = 2.5$ cm s^{-1} and was directed along the x-axis. The buoyancy frequency was $N = 1.0 \times 10^{-3}$ s^{-1}. Figure 9 presented the variations of the conversion with c in log–log representation and figure 10 the associated slopes. As long as the seamount was subcritical, the conversion followed the WTA prediction as c^2. At $c = 1000$ m, the seamount became supercritical and the slope of the log–log plot jumped to 2.5 for $\epsilon_h' < 0.5$ and to higher values for $0.5 < \epsilon_h' < 1$, up to 3.5 for $\epsilon_h' = 1$. At $c = 1500$ m, the slope started to fall down, a saturation all the more pronounced that ϵ_h' was close to 1.
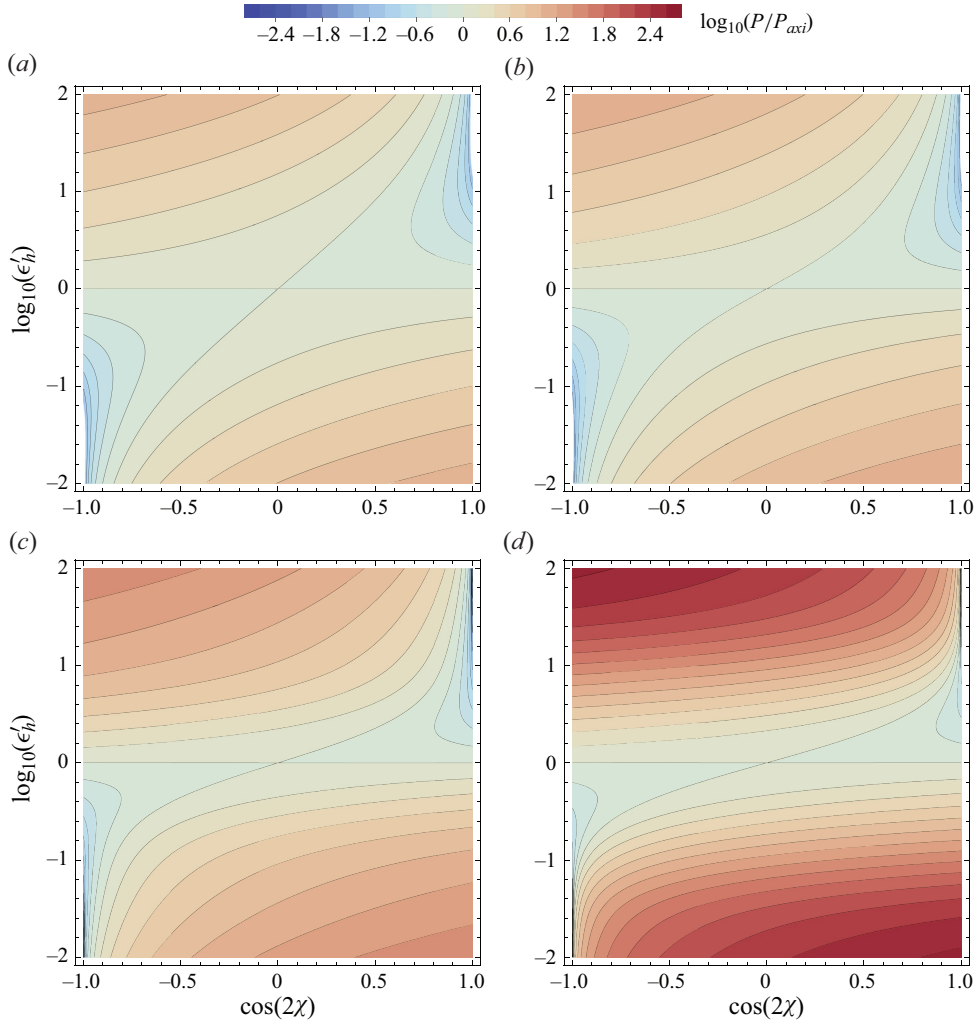
Figure 15. Variations of the asymmetry factor of (*a*) a weak Gaussian seamount and ellipsoidal seamounts of (*b*) $\Upsilon'_v = 1$, (*c*) $\Upsilon'_v = 2$ and (*d*) $\Upsilon'_v = 5$, with the direction of barotropic oscillation and with the horizontal aspect ratio of the seamount.

The present figure 16(*a*) shows the WTA prediction for this seamount, and figure 16(*b*) the exact prediction for the equivalent ellipsoid, taking $\rho_0 = 1025$ kg m^{-3}, typical of sea water. In both cases, the order of magnitude of the conversion is similar to that obtained numerically, consistent with the prediction by Baines (2007) of an energy flux of order 1 MW for barotropic tidal flow of 1 cm s^{-1} amplitude over a pillbox-shaped seamount. Saturation is seen to be all the more pronounced, and to happen all the sooner, when the ellipsoid is close to axisymmetric. Therefore, supercriticality appears as a decisive factor in the occurrence of saturation, even in the absence of nonlinear effects.

5.3. *The weak-topography approximation revisited*

Nycander (2005) introduced an original method for calculating the conversion on a global scale, based on the WTA. The conversion was written as (1.1) in spectral space and (1.3)
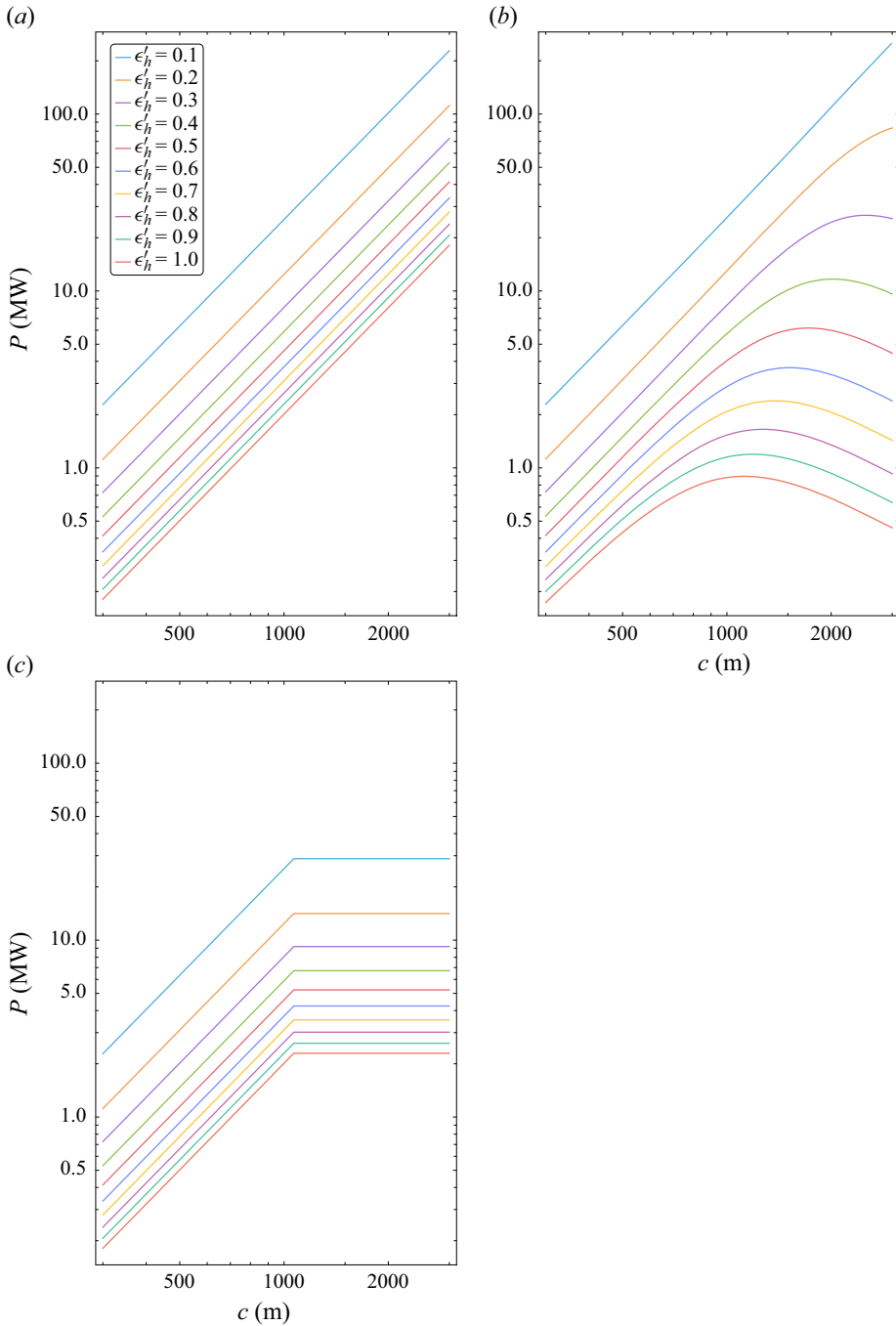
999 A59-30

Figure 16. Conversion rate for the seamount in figure 9 of Munroe & Lamb (2005), modelled as (*a*) a weak Gaussian seamount, (*b*) an ellipsoidal seamount and (*c*) a weak Gaussian seamount corrected for supercriticality. The seamount has fixed radius $a = 4.56$ km along the *x*-axis, and variable aspect ratio $\epsilon'_h = a/b$ and height *c*.

in direct space, and the finite ocean depth was taken into account in a heuristic way, based on the WKB analysis of Llewellyn Smith & Young (2002), by multiplying the integrand of (1.1) by a high-pass filter excluding the contribution of the topographic scales larger than the horizontal wavelength of the first internal wave mode, and changing the kernel of (1.3) accordingly. Approximately half the global conversion came from supercritical slopes and was known to be overestimated. Green & Nycander (2013) came out with an improved numerical scheme and dealt with supercriticality by capping the conversion at 1 W m^{-2}.

Melet *et al.* (2013) and Falahat *et al.* (2014) built upon this work, for the former by comparing direct- and spectral-space approaches, and for the latter by comparing the heuristic approach of finite depth with a full calculation in vertical modes, allowing also $N(z)$ to vary. Both introduced a two-tier correction to the WTA, dividing first the contribution of supercritical slopes by the squared steepness ratio γ^2, then capping the outcome at 1 W m^{-2} in shallow seas. As a result, the global conversion was reduced by 20 %–30 %. Vic *et al.* (2019, Supplementary note 1) looked at the two corrections more closely, and found that the first is at work at depths shallower than 2000 m, while the second only affects regions shallower than 700 m.

For the Gaussian seamount in table 2, the maximum slope for $a < b$ is $c/(a\sqrt{e})$, reached at $(x = \pm a, y = 0)$, such that $\gamma = c/(a\sqrt{e})(N^2/\omega^2 - 1)^{1/2}$. Applying the first correction above, namely dividing P_{axi} by γ^2 when $\gamma > 1$, gives

$$\frac{\pi^{3/2}e}{8}\rho_0 \frac{\omega^2}{(N^2 - \omega^2)^{1/2}} a^{5/2}b^{1/2}(U^2 + V^2). \tag{5.8}$$

The conversion is now independent of c, yielding the saturation in figure 16(*c*). The second correction, taking $\pi ab = \pi a^2/\epsilon_h'$ as the horizontal area of the seamount, caps the conversion at $65.3/\epsilon_h'$ MW and does not play a role in the parameter range of the figure.

Comparison with the ellipsoid in figure 16(*b*) shows that the corrections account for the saturation that arises as the seamount becomes supercritical, but not for the decrease of the conversion afterwards. They also do not account for the delayed occurrence of saturation as the topography gets two-dimensional, namely as ϵ_h' decreases. This may be a consequence of the simplistic way in which the corrections to the WTA have been applied, considering the seamount as a single entity and applying the corrections to it as a whole. A better comparison would require the implementation of the numerical scheme described in the appendix of Green & Nycander (2013), and then to proceed as for the diagonal ridge there; namely, to consider a domain that is large compared with the size of the seamount (say of 50 times its radii in the x and y directions), subdivide this domain into cells that are small compared with that size (say of 1/10th the radii), then apply the corrections only to the cells where the slopes are supercritical. This falls outside the scope of the present study.

6. Conclusion

This paper has dealt with two aspects of the generation of internal waves by oscillating bodies. The first aspect is the modelling of the generation process. Voisin (2021) developed a representation of the bodies by the boundary integral method, and Voisin (2024) investigated the link of this representation to added mass, providing immediate access to the impulse response function of the bodies and to their radiated energy. The method was implemented for an elliptic cylinder of horizontal axis, using elliptic coordinates and circular harmonics, and for a spheroid of vertical axis, using spheroidal coordinates and spherical harmonics.

999 A59-32

The present paper has extended this approach to a triaxial ellipsoid, using ellipsoidal coordinates and ellipsoidal harmonics, based on the presentations of these harmonics by Hobson (1931, chapter 11) and Dassios (2012). The extension, in §§ 2–4, has confirmed the behaviours already observed for the spheroid, and clarified the transition from three to two dimensions. The peculiar behaviours observed for the cylinder – no inertial added mass in the frequency range of propagating waves and an everlasting memory for the impulse response function, all independent from the direction of motion – emerge as limits of the behaviours observed for the ellipsoid. The radiated power exhibits, for fixed oscillation amplitude, a maximum at 0.8 to 1 times the buoyancy frequency, for ellipsoids that are horizontally flat and vertically elongated, respectively.

The second aspect is the application of the analysis to the conversion of barotropic tidal energy into baroclinic form, when tidal oscillations take place over topography at the bottom of the stratified ocean; a problem amenable, for small tidal excursion, to the generation of internal waves by the oscillations of the topography in a stratified ocean at rest. In actuality, the waves form beams affected by viscous and turbulent effects as they propagate away from the topography (see Voisin *et al.* 2011 and Voisin 2020, and the references therein), and the interactions of these beams with themselves and with the boundary layer generate sub- and superharmonics (see Korobov & Lamb 2008). However, the radiated wave power, called conversion rate in this context, depends only on the coupling of the barotropic and baroclinic oscillations by the free-slip condition at the topography, modelled by the boundary integral method.

A fundamental difference arises between sub- and supercritical topographies, namely topographies of slopes smaller and larger than the slope of the wave rays, respectively. For the former, Llewellyn Smith & Young (2002) developed a model based on the weak-topography approximation, assuming the topographic slope to be much smaller than the ray slope, and predicting a variation of the conversion as the square of the topographic height. This model formed the basis of the global calculations of the conversion by Nycander (2005), Green & Nycander (2013), Melet *et al.* (2013), Falahat *et al.* (2014) and Vic *et al.* (2019), who introduced a two-tier heuristic correction for supercriticality. The present § 5 is the first analytical study of three-dimensional supercritical topography, since the study of a vertical pillbox in a finite-depth ocean by Baines (2007) and a spherical seamount in a semi-infinite ocean by Voisin *et al.* (2011). The conclusions of Llewellyn Smith & Young (2002) on the effect of the horizontal anisotropy of the seamount have been confirmed, and shown to be amplified by supercriticality. Application in figure 16 to the seamount considered numerically by Munroe & Lamb (2005), representative of the topography near the Hawaiian islands, shows a saturation of the conversion, then a decrease, as the height of the seamount increases. The heuristic correction to the WTA, at least in the simple form used in § 5.3, reproduces these effects only partially and does not account for their disappearance as the topography gets two-dimensional.

A limitation of the analysis is the unrealistic representation of the ocean, assumed to be of infinite depth and uniformly stratified, and to a lesser extent, the neglect of the rotation of the Earth. With finite depth and non-uniform stratification, the waves decompose into vertical normal modes. The inclusion of these modes has been discussed by Llewellyn Smith & Young (2002) for isolated seamounts and Falahat *et al.* (2014) for global bathymetry, in the context of the weak-topography approximation. Stronger topographies may lead to mode coupling, discussed by Papoutsellis *et al.* (2023) who also provide an up-to-date bibliography on the internal tide. Finally, it must be noted that the attention of the oceanographic community, focused for approximately two decades on the

total conversion, has recently moved to the direction of the energy flux (Pollmann *et al.* 2019).

Author ORCID.
Ⓓ Bruno Voisin https://orcid.org/0000-0002-3741-3840.

Appendix A. Ellipsoidal harmonics

This appendix is based on Hobson (1931, chapter 11) and Dassios (2012). Compared with the latter, the surface harmonics have been normalized.

A.1. *Ellipsoidal coordinates*

The reference ellipsoid has, in Cartesian coordinates (x, y, z), the equation

$$\frac{x^2}{a^2} + \frac{y^2}{b^2} + \frac{z^2}{c^2} = 1, \tag{A1}$$

the semi-axes $a > b > c$ and the semi-focal distances

$$h_1 = (b^2 - c^2)^{1/2}, \quad h_2 = (a^2 - c^2)^{1/2}, \quad h_3 = (a^2 - b^2)^{1/2}, \tag{A2a–c}$$

with $h_2 > h_1$ and $h_2 > h_3$. The ellipsoidal coordinates (ρ, μ, ν) are defined by

$$x = \frac{\rho\mu\nu}{h_2 h_3}, \tag{A3a}$$

$$y = \frac{(\rho^2 - h_3^2)^{1/2}(\mu^2 - h_3^2)^{1/2}(h_3^2 - \nu^2)^{1/2}}{h_1 h_3}, \tag{A3b}$$

$$z = \frac{(\rho^2 - h_2^2)^{1/2}(h_2^2 - \mu^2)^{1/2}(h_2^2 - \nu^2)^{1/2}}{h_1 h_2}, \tag{A3c}$$

where the coordinates and square roots on the right-hand sides take positive values, with $\rho > h_2 > \mu > h_3 > \nu$, save for

$$\text{sign}\,\nu = \text{sign}\,x, \quad \text{sign}(h_3^2 - \nu^2)^{1/2} = \text{sign}\,y, \quad \text{sign}(h_2^2 - \mu^2)^{1/2} = \text{sign}\,z. \tag{A4a–c}$$

The surfaces of constant ρ are confocal ellipsoids, and the surfaces of constant μ and ν are confocal hyperboloids of one and two sheets, respectively. Accordingly, ρ acts as a radial coordinate and (μ, ν) as angular coordinates.

The metric coefficients are

$$h_\rho = \frac{(\rho^2 - \mu^2)^{1/2}(\rho^2 - \nu^2)^{1/2}}{(\rho^2 - h_2^2)^{1/2}(\rho^2 - h_3^2)^{1/2}}, \tag{A5a}$$

$$h_\mu = \frac{(\rho^2 - \mu^2)^{1/2}(\mu^2 - \nu^2)^{1/2}}{(h_2^2 - \mu^2)^{1/2}(\mu^2 - h_3^2)^{1/2}}, \tag{A5b}$$

$$h_\nu = \frac{(\rho^2 - \nu^2)^{1/2}(\mu^2 - \nu^2)^{1/2}}{(h_2^2 - \nu^2)^{1/2}(h_3^2 - \nu^2)^{1/2}}. \tag{A5c}$$

The unit vectors $(\boldsymbol{e}_\rho, \boldsymbol{e}_\mu, \boldsymbol{e}_\nu)$ are related to those $(\boldsymbol{e}_x, \boldsymbol{e}_y, \boldsymbol{e}_z)$ for the Cartesian system by

$$\boldsymbol{e}_\rho = \frac{\rho}{h_\rho}\left(\frac{x}{\rho^2}\boldsymbol{e}_x + \frac{y}{\rho^2 - h_3^2}\boldsymbol{e}_y + \frac{z}{\rho^2 - h_2^2}\boldsymbol{e}_z\right), \tag{A6a}$$

$$\boldsymbol{e}_\mu = \frac{\mu}{h_\mu}\left(\frac{x}{\mu^2}\boldsymbol{e}_x + \frac{y}{\mu^2 - h_3^2}\boldsymbol{e}_y + \frac{z}{\mu^2 - h_2^2}\boldsymbol{e}_z\right), \tag{A6b}$$

$$\boldsymbol{e}_\nu = \frac{\nu}{h_\nu}\left(\frac{x}{\nu^2}\boldsymbol{e}_x + \frac{y}{\nu^2 - h_3^2}\boldsymbol{e}_y + \frac{z}{\nu^2 - h_2^2}\boldsymbol{e}_z\right). \tag{A6c}$$

The gradient operator is

$$\boldsymbol{\nabla} = \frac{\boldsymbol{e}_\rho}{h_\rho}\frac{\partial}{\partial\rho} + \frac{\boldsymbol{e}_\mu}{h_\mu}\frac{\partial}{\partial\mu} + \frac{\boldsymbol{e}_\nu}{h_\nu}\frac{\partial}{\partial\nu}. \tag{A7}$$

On an ellipsoid of constant ρ, the solid angle element is

$$\mathrm{d}\varpi = \frac{\mu^2 - \nu^2}{(h_2^2 - \mu^2)^{1/2}(\mu^2 - h_3^2)^{1/2}(h_2^2 - \nu^2)^{1/2}(h_3^2 - \nu^2)^{1/2}}\,\mathrm{d}\mu\,\mathrm{d}\nu. \tag{A8}$$

Introduction of the eccentric angles (ϑ, φ), such that

$$\cos\vartheta = \frac{\mu\nu}{h_2 h_3}, \tag{A9a}$$

$$\sin\vartheta\cos\varphi = \frac{(\mu^2 - h_3^2)^{1/2}(h_3^2 - \nu^2)^{1/2}}{h_1 h_3}, \tag{A9b}$$

$$\sin\vartheta\sin\varphi = \frac{(h_2^2 - \mu^2)^{1/2}(h_2^2 - \nu^2)^{1/2}}{h_1 h_2}, \tag{A9c}$$

transforms the ellipsoid into the spherical domain $(0 < \vartheta < \pi, 0 < \varphi < 2\pi)$, and the solid angle element into

$$\mathrm{d}\varpi = \sin\vartheta\,\mathrm{d}\vartheta\,\mathrm{d}\varphi, \tag{A10}$$

its familiar expression in the spherical direction (ϑ, φ). Ellipto-spherical coordinates $(\rho, \vartheta, \varphi)$ follow, defined by

$$x = \rho\cos\vartheta, \quad y = (\rho^2 - h_3^2)^{1/2}\sin\vartheta\cos\varphi, \quad z = (\rho^2 - h_2^2)^{1/2}\sin\vartheta\sin\varphi. \tag{A11a–c}$$

In contrast to the ellipsoidal system, the ellipto-spherical system is not orthogonal. Accordingly, ellipsoidal coordinates are better suited for calculating gradients and normal derivatives, and ellipto-spherical coordinates for evaluating surface integrals.

The reference ellipsoid is the surface $\rho = a$, with the outward normal

$$\boldsymbol{n} = \frac{abc}{(a^2 - \mu^2)^{1/2}(a^2 - \nu^2)^{1/2}} \left(\frac{x}{a^2}\boldsymbol{e}_x + \frac{y}{b^2}\boldsymbol{e}_y + \frac{z}{c^2}\boldsymbol{e}_z \right), \tag{A12}$$

the normal derivative

$$\frac{\partial}{\partial n} = \frac{bc}{(a^2 - \mu^2)^{1/2}(a^2 - \nu^2)^{1/2}} \frac{\partial}{\partial \rho}, \tag{A13}$$

and the surface area element

$$\mathrm{d}^2 S = (a^2 - \mu^2)^{1/2}(a^2 - \nu^2)^{1/2} \, \mathrm{d}\varpi. \tag{A14}$$

In terms of the eccentric angles, we have, on the reference ellipsoid,

$$x = a\cos\vartheta, \quad x = b\sin\vartheta\cos\varphi, \quad x = c\sin\vartheta\sin\varphi, \tag{A15a–c}$$

bringing out the analogy with the eccentric angle for an ellipse in two dimensions.

A.2. *Lamé functions*

The solution of the Laplace equation with respect to the coordinate ρ involves the Lamé functions, which are either interior, $E_l^m(\rho)$, varying as ρ^l at infinity, or exterior, $F_l^m(\rho)$, varying as $1/\rho^{l+1}$. The two types of functions are related by

$$F_l^m(\rho) = (2l + 1)E_l^m(\rho)I_l^m(\rho), \tag{A16}$$

where

$$I_l^m(\rho) = \int_\rho^\infty \frac{\mathrm{d}t}{[E_l^m(t)]^2(t^2 - h_2^2)^{1/2}(t^2 - h_3^2)^{1/2}}. \tag{A17}$$

The degree l takes the integer values $0, 1, 2, \ldots$, and the index m the values $1, 2, \ldots, 2l + 1$.

The elliptic integrals $I_l^m(\rho)$ may be expressed in terms of the Legendre integrals

$$E(\alpha, \beta) = \int_0^\alpha (1 - \beta\sin^2\theta)^{1/2} \, \mathrm{d}\theta, \quad F(\alpha, \beta) = \int_0^\alpha \frac{\mathrm{d}\theta}{(1 - \beta\sin^2\theta)^{1/2}}, \tag{A18a,b}$$

for which the definition by Abramowitz & Stegun (1972, chapter 17) has been used, involving the parameter β, rather than the definition by Olver *et al.* (2010, chapter 19), involving the modulus $\beta^{1/2}$. This was done to avoid the complications that would arise otherwise with the determination of the square root $\beta^{1/2}$ in (3.15). This is also the definition implemented by MATHEMATICA. For $\alpha = \pi/2$, the Legendre integrals have

the complete forms

$$E(\beta) = E\left(\frac{\pi}{2}, \beta\right), \quad K(\beta) = F\left(\frac{\pi}{2}, \beta\right). \tag{A19a,b}$$

For $\beta \to 0$, they expand as

$$E(\alpha, \beta) \sim \alpha - \frac{\beta}{4}(\alpha - \sin\alpha\cos\alpha), \quad F(\alpha, \beta) \sim \alpha + \frac{\beta}{4}(\alpha - \sin\alpha\cos\alpha), \tag{A20a,b}$$

and for $\beta \to 1$, as

$$E(\alpha, \beta) \sim \sin\alpha + \frac{1-\beta}{2}[\operatorname{arctanh}(\sin\alpha) - \sin\alpha], \tag{A21a}$$

$$F(\alpha, \beta) \sim \operatorname{arctanh}(\sin\alpha) + \frac{1-\beta}{4}\left[\operatorname{arctanh}(\sin\alpha) - \frac{\sin\alpha}{\cos^2\alpha}\right]. \tag{A21b}$$

For $l = 0$, we have

$$E_0^1(\rho) = 1, \quad I_0^1(\rho) = \frac{F(\alpha, \beta)}{h_2}, \tag{A22a,b}$$

where

$$\alpha = \arcsin\left(\frac{h_2}{\rho}\right), \quad \beta = \frac{h_3^2}{h_2^2}. \tag{A23a,b}$$

For $l = 1$, we have

$$E_1^1(\rho) = \rho, \quad E_1^2(\rho) = (\rho^2 - h_3^2)^{1/2}, \quad E_1^3(\rho) = (\rho^2 - h_2^2)^{1/2}, \tag{A24a–c}$$

together with

$$I_1^1(\rho) = \frac{F(\alpha, \beta) - E(\alpha, \beta)}{h_2 h_3^2}, \tag{A25a}$$

$$I_1^2(\rho) = \frac{E(\alpha, \beta)/(1-\beta) - F(\alpha, \beta)}{h_2 h_3^2} - \frac{1}{h_1^2 \rho} \frac{(\rho^2 - h_2^2)^{1/2}}{(\rho^2 - h_3^2)^{1/2}}, \tag{A25b}$$

$$I_1^3(\rho) = \frac{1}{h_1^2 \rho} \frac{(\rho^2 - h_3^2)^{1/2}}{(\rho^2 - h_2^2)^{1/2}} - \frac{E(\alpha, \beta)}{h_1^2 h_2}. \tag{A25c}$$

A.3. *Surface harmonics*

The solution of the Laplace equation with respect to the coordinates μ and ν involves the surface harmonics

$$S_l^m(\mu, \nu) = \frac{E_l^m(\mu) E_l^m(\nu)}{\sqrt{\gamma_l^m}}, \tag{A26}$$

with the normalization constant

$$\gamma_l^m = \int_{\rho=a} [E_l^m(\mu) E_l^m(\nu)]^2 \, d\varpi. \tag{A27}$$

The surface harmonics are orthogonal over any ellipsoid of constant ρ. They are normalized over the reference ellipsoid $\rho = a$, where they satisfy

$$\int_{\rho=a} S_l^m(\mu, \nu) S_{l'}^{m'}(\mu, \nu) \, d\varpi = \delta_{ll'} \delta_{mm'}, \tag{A28}$$

with δ_{ij} the Kronecker delta symbol. Any function $g(\mu, \nu)$ may be expanded in the form

$$g(\mu, \nu) = \sum_{l=0}^{\infty} \sum_{m=1}^{2l+1} g_{lm} S_l^m(\mu, \nu), \tag{A29}$$

with

$$g_{lm} = \int_{\rho=a} g(\mu, \nu) S_l^m(\mu, \nu) \, d\varpi. \tag{A30}$$

Alternatively, the surface harmonics may be expressed in terms of the eccentric angles. We denote this expression as $s_l^m(\vartheta, \varphi) = S_l^m(\mu, \nu)$. The orthonormality relation (A28) becomes

$$\int_0^{2\pi} \int_0^{\pi} s_l^m(\vartheta, \varphi) s_{l'}^{m'}(\vartheta, \varphi) \sin \vartheta \, d\vartheta \, d\varphi = \delta_{ll'} \delta_{mm'}, \tag{A31}$$

and the expansion (A29) becomes

$$g(\mu, \nu) = \sum_{l=0}^{\infty} \sum_{m=1}^{2l+1} g_{lm} s_l^m(\vartheta, \varphi), \tag{A32}$$

where

$$g_{lm} = \int_0^{2\pi} \int_0^{\pi} g(\mu, \nu) s_l^m(\vartheta, \varphi) \sin \vartheta \, d\vartheta \, d\varphi. \tag{A33}$$

For $l = 0$, we have

$$s_0^1(\vartheta, \varphi) = \sqrt{\frac{1}{4\pi}}, \tag{A34}$$

and for $l = 1$, we have

$$s_1^1(\vartheta, \varphi) = \sqrt{\frac{3}{4\pi}} \cos \vartheta, \tag{A35a}$$

$$s_1^2(\vartheta, \varphi) = \sqrt{\frac{3}{4\pi}} \sin \vartheta \cos \varphi, \tag{A35b}$$

$$s_1^3(\vartheta, \varphi) = \sqrt{\frac{3}{4\pi}} \sin \vartheta \sin \varphi. \tag{A35c}$$

A.4. *Green's function*

Together, the Lamé functions and the surface harmonics form solid ellipsoidal harmonics. For two points x and x' of respective ellipsoidal coordinates (ρ, μ, ν) and (ρ', μ', ν'), the Green's function of the Laplace equation has the expansion

$$\frac{1}{|x - x'|} = 4\pi \sum_{l=0}^{\infty} \sum_{m=1}^{2l+1} E_l^m(\rho_<) E_l^m(\rho_>) I_l^m(\rho_>) S_l^m(\mu, \nu) S_l^m(\mu', \nu'), \qquad (A36)$$

or equivalently, in ellipto-spherical coordinates $(\rho, \vartheta, \varphi)$ and $(\rho', \vartheta', \varphi')$,

$$\frac{1}{|x - x'|} = 4\pi \sum_{l=0}^{\infty} \sum_{m=1}^{2l+1} E_l^m(\rho_<) E_l^m(\rho_>) I_l^m(\rho_>) s_l^m(\vartheta, \varphi) s_l^m(\vartheta', \varphi'), \qquad (A37)$$

where $\rho_< = \min(\rho, \rho')$ and $\rho_> = \max(\rho, \rho')$.

REFERENCES

ABRAMOWITZ, M. & STEGUN, I.A. 1972 *Handbook of Mathematical Functions*, 10th edn. Dover.
BAINES, P.G. 1973 The generation of internal tides by flat-bump topography. *Deep-Sea Res.* **20**, 179–205.
BAINES, P.G. 1974 The generation of internal tides over steep continental slopes. *Phil. Trans. R. Soc. Lond.* A **277**, 27–58.
BAINES, P.G. 1982 On internal tide generation models. *Deep-Sea Res.* A **29**, 307–338.
BAINES, P.G. 2007 Internal tide generation by seamounts. *Deep-Sea Res.* I **5**, 1486–1508.
BALMFORTH, N.J., IERLEY, G.R. & YOUNG, W.R. 2002 Tidal conversion by subcritical topography. *J. Phys. Oceanogr.* **32**, 2900–2914.
BALMFORTH, N.J. & PEACOCK, T. 2009 Tidal conversion by supercritical topography. *J. Phys. Oceanogr.* **39**, 1965–1974.
BATCHELOR, G.K. 1967 *An Introduction to Fluid Dynamics*. Cambridge University Press.
BECKMANN, A. & HAIDVOGEL, D.B. 1993 Numerical simulation of flow around a tall isolated seamount. Part I. Problem formulation and model accuracy. *J. Phys. Oceanogr.* **23**, 1736–1753.
BELL, T.H. 1975a Lee waves in stratified flows with simple harmonic time dependence. *J. Fluid Mech.* **67**, 705–722.
BELL, T.H. 1975b Topographically generated internal waves in the open ocean. *J. Geophys. Res.* **80**, 320–327.
BRYAN, G.H. 1889 The waves on a rotating liquid spheroid of finite ellipticity. *Phil. Trans. R. Soc. Lond.* A **180**, 187–219.
BÜHLER, O. & MULLER, C.J. 2007 Instability and focusing of internal tides in the deep ocean. *J. Fluid Mech.* **588**, 1–28.
COX, C. & SANDSTROM, H. 1962 Coupling of internal and surface waves in water of variable depth. In *Journal of the Oceanographical Society of Japan, 20th Anniversary Volume*, pp. 499–513. Oceanographical Society of Japan.
CRAIG, P.D. 1987 Solution for internal tide generation over coastal topography. *J. Mar. Res.* **45**, 83–105.
CUMMINS, W.E. 1962 The impulse response function and ship motions. *Schiffstechnik* **9**, 101–109.
DAI, D., WANG, W., ZHANG, Q., QIAO, F. & YUAN, Y. 2011 Eigen solutions of internal waves over subcritical topography. *Acta Oceanol. Sin.* **30**, 1–8.
DASSIOS, G. 2012 *Ellipsoidal Harmonics: Theory and Applications*. Cambridge University Press.
DETTNER, A., SWINNEY, H.L. & PAOLETTI, M.S. 2013 Internal wave and boundary current generation by tidal flow over topography. *Phys. Fluids* **25**, 116601.
DI LORENZO, E., YOUNG, W.R. & LLEWELLYN SMITH, S. 2006 Numerical and analytical estimates of M_2 tidal conversion at steep oceanic ridges. *J. Phys. Oceanogr.* **36**, 1072–1084.
DOSSMANN, Y., PACI, A., AUCLAIR, F. & FLOOR, J.W. 2011 Simultaneous velocity and density measurements for an energy-based approach to internal waves generated over a ridge. *Exp. Fluids* **51**, 1013–1028.
ECHEVERRI, P., FLYNN, M.R., WINTERS, K.B. & PEACOCK, T. 2009 Low-mode internal tide generation by topography: an experimental and numerical investigation. *J. Fluid Mech.* **636**, 91–108.
ECHEVERRI, P. & PEACOCK, T. 2010 Internal tide generation by arbitrary two-dimensional topography. *J. Fluid Mech.* **659**, 247–266.

ERMANYUK, E.V. 2002 The rule of affine similitude for the force coefficients of a body oscillating in a uniformly stratified fluid. *Exp. Fluids* **32**, 242–251.

ERMANYUK, E.V., FLÓR, J.-B. & VOISIN, B. 2011 Spatial structure of first and higher harmonic internal waves from a horizontally oscillating sphere. *J. Fluid Mech.* **671**, 364–383.

ERMANYUK, E.V. & GAVRILOV, N.V. 2008 On internal waves generated by large-amplitude circular and rectilinear oscillations of a circular cylinder in a uniformly stratified fluid. *J. Fluid Mech.* **613**, 329–356.

FALAHAT, S., NYCANDER, J., ROQUET, F. & ZARROUG, M. 2014 Global calculation of tidal energy conversion into vertical normal modes. *J. Phys. Oceanogr.* **44**, 3225–3244.

FERRARI, R., MASHAYEK, A., MCDOUGALL, T.J., NIKURASHIN, M. & CAMPIN, J. 2016 Turning ocean mixing upside down. *J. Phys. Oceanogr.* **46**, 2239–2261.

FERRARI, R. & WUNSCH, C. 2009 Ocean circulation kinetic energy: reservoirs, sources, and sinks. *Annu. Rev. Fluid Mech.* **41**, 253–282.

FLOOR, J.W., AUCLAIR, F. & MARSALEIX, P. 2011 Energy transfers in internal tide generation, propagation and dissipation in the deep ocean. *Ocean Model.* **38**, 22–40.

GABOV, S.A. & KRUTITSKII, P.A. 1987 On the non-stationary Larsen problem. *USSR Comput. Maths Math. Phys.* **27** (4), 148–154.

GARRETT, C. & GERKEMA, T. 2007 On the body-force term in internal-tide generation. *J. Phys. Oceanogr.* **37**, 2172–2175.

GARRETT, C. & KUNZE, E. 2007 Internal tide generation in the deep ocean. *Annu. Rev. Fluid Mech.* **39**, 57–87.

GÖRTLER, H. 1943 Über eine Schwingungserscheinung in Flüssigkeiten mit stabiler Dichteschichtung. *Z. Angew. Math. Mech.* **23**, 65–71.

GREEN, J.A.M. & NYCANDER, J. 2013 A comparison of tidal conversion parameterizations for tidal models. *J. Phys. Oceanogr.* **43**, 104–119.

GRIFFITHS, S.D. & GRIMSHAW, R.H.J. 2007 Internal tide generation at the continental shelf modeled using a modal decomposition: two-dimensional results. *J. Phys. Oceanogr.* **37**, 428–451.

GUSTAFSSON, K.E. 2001 Computations of the energy flux to mixing processes via baroclinic wave drag on barotropic tides. *Deep-Sea Res.* I **48**, 2283–2295.

HAIDVOGEL, D.B., BECKMANN, A., CHAPMAN, D.C. & LIN, R.-Q. 1993 Numerical simulation of flow around a tall isolated seamount. Part II. Resonant generation of trapped waves. *J. Phys. Oceanogr.* **23**, 2373–2391.

HOBSON, E.W. 1931 *The Theory of Spherical and Ellipsoidal Harmonics*. Cambridge University Press.

HOLLOWAY, P.E. & MERRIFIELD, M.A. 1999 Internal tide generation by seamounts, ridges, and islands. *J. Geophys. Res.* C **104**, 25937–25951.

HURLEY, D.G. 1972 A general method for solving steady-state internal gravity wave problems. *J. Fluid Mech.* **56**, 721–740.

JACKSON, J.D. 1999 *Classical Electrodynamics*, 3rd edn. Wiley.

JALALI, M., RAPAKA, N.R. & SARKAR, S. 2014 Tidal flow over topography: effect of excursion number on wave energetics and turbulence. *J. Fluid Mech.* **750**, 259–283.

JALALI, M., VANDINE, A., CHALAMALLA, V.K. & SARKAR, S. 2017 Oscillatory stratified flow over supercritical topography: wave energetics and turbulence. *Comput. Fluids* **158**, 39–48.

JIA, X., CHEN, X., LI, Q. & LI, Q. 2014 Study on internal waves generated by tidal flow over critical topography. *J. Ocean Univ. China* **13**, 728–732.

KHATIWALA, S. 2003 Generation of internal tides in an ocean of finite depth: analytical and numerical calculations. *Deep-Sea Res.* I **50**, 3–21.

KING, B., ZHANG, H.P. & SWINNEY, H.L. 2009 Tidal flow over three-dimensional topography in a stratified fluid. *Phys. Fluids* **21**, 116601.

KING, B., ZHANG, H.P. & SWINNEY, H.L. 2010 Tidal flow over three-dimensional topography generates out-of-forcing-plane harmonics. *Geophys. Res. Lett.* **37**, L14606.

KOCHIN, N.E., KIBEL', I.A. & ROZE, N.V. 1964 *Theoretical Hydromechanics*. Wiley.

KOROBOV, A.S. & LAMB, K.G. 2008 Interharmonics in internal gravity waves generated by tide–topography interaction. *J. Fluid Mech.* **611**, 61–95.

KOROTKIN, A.I. 2009 *Added Masses of Ship Structures*. Springer.

KRUTITSKII, P.A. 1988 Small non-stationary vibrations of vertical plates in a channel with a stratified liquid. *USSR Comput. Maths Math. Phys.* **28** (6), 166–176.

LAMB, H. 1932 *Hydrodynamics*, 6th edn. Cambridge University Press.

LAMB, K.G. 2004 Nonlinear interaction among internal wave beams generated by tidal flow over supercritical topography. *Geophys. Res. Lett.* **31**, L09313.

LANDAU, L.D. & LIFSHITZ, E.M. 1987 *Fluid Mechanics*, 2nd edn. Pergamon.

LE DIZÈS, S. 2024 Critical slope singularities in rotating and stratified fluids. *Phys. Rev. Fluids* **9**, 034803.

LE DIZÈS, S. & LE BARS, M. 2017 Internal shear layers from librating objects. *J. Fluid Mech.* **826**, 653–675.

LEE, F.M., PAOLETTI, M.S., SWINNEY, H.L. & MORRISON, P.J. 2014 Experimental determination of radiated internal wave power without pressure field data. *Phys. Fluids* **26**, 046606.

LEGG, S. & HUIJTS, K.M.H. 2006 Preliminary simulations of internal waves and mixing generated by finite amplitude tidal flow over isolated topography. *Deep-Sea Res.* II **53**, 140–156.

LEGG, S. & KLYMAK, J. 2008 Internal hydraulic jumps and overturning generated by tidal flow over a tall steep ridge. *J. Phys. Oceanogr.* **38**, 1949–1964.

LIGHTHILL, J. 1986 *An Informal Introduction to Theoretical Fluid Mechanics*. Oxford University Press.

LLEWELLYN SMITH, S.G. & YOUNG, W.R. 2002 Conversion of the barotropic tide. *J. Phys. Oceanogr.* **32**, 1554–1566.

LLEWELLYN SMITH, S.G. & YOUNG, W.R. 2003 Tidal conversion at a very steep ridge. *J. Fluid Mech.* **495**, 175–191.

MAAS, L.R.M. 2011 Topographies lacking tidal conversion. *J. Fluid Mech.* **684**, 5–24.

MARTIN, P.A. 2006 *Multiple Scattering*. Cambridge University Press.

MATHUR, M., CARTER, G.S. & PEACOCK, T. 2016 Internal tide generation using Green function analysis: to WKB or not to WKB? *J. Phys. Oceanogr.* **46**, 2157–2168.

MAUGÉ, R. & GERKEMA, T. 2008 Generation of weakly nonlinear nonhydrostatic internal tides over large topography: a multi-modal approach. *Nonlinear Process. Geophys.* **15**, 233–244.

MELET, A., NIKURASHIN, M., MULLER, C., FALAHAT, S., NYCANDER, J., TIMKO, P.G., ARBIC, B.K. & GOFF, J.A. 2013 Internal tide generation by abyssal hills using analytical theory. *J. Geophys. Res. Oceans* **118**, 6303–6318.

MILNE-THOMSON, L.M. 1968 *Theoretical Hydrodynamics*, 5th edn. Dover.

MOROZOV, E.G. 1995 Semidiurnal internal wave global field. *Deep-Sea Res.* I **42**, 135–148.

MOROZOV, E. 2006 Internal tides. Global field of internal tides and mixing caused by internal tides. In *Waves in Geophysical Fluids. Tsunamis, Rogue Waves, Internal Waves and Internal Tides* (ed. J. Grue & K. Trulsen), pp. 271–332. Springer.

MOROZOV, E.G. 2018 *Oceanic Internal Tides: Observations, Analysis and Modeling*. Springer.

MOWBRAY, D.E. & RARITY, B.S.H. 1967 A theoretical and experimental investigation of the phase configuration of internal waves of small amplitude in a density stratified liquid. *J. Fluid Mech.* **28**, 1–16.

MUNROE, J.R. & LAMB, K.G. 2005 Topographic amplitude dependence of internal wave generation by tidal forcing over idealized three-dimensional topography. *J. Geophys. Res.* C **110**, 02001.

NEWMAN, J.N. 2017 *Marine Hydrodynamics*, 40th edn. MIT Press.

NYCANDER, J. 2005 Generation of internal waves in the deep ocean by tides. *J. Geophys. Res.* **110**, C10028.

NYCANDER, J. 2006 Tidal generation of internal waves from a periodic array of steep ridges. *J. Fluid Mech.* **567**, 415–432.

OGILVIE, T.F. 1964 Recent progress toward the understanding and prediction of ship motions. In *Proceedings of the 5th Symposium on Naval Hydrodynamics* (ed. J.K. Lunde & S.W. Doroff), pp. 3–80. U.S. Government Printing Office. Available at: http://resolver.tudelft.nl/uuid:73776ccf-258f-4d5d-ab6c-88c95a002091.

OLVER, F.W.J., LOZIER, D.W., BOISVERT, R.F. & CLARK, C.W. 2010 *NIST Handbook of Mathematical Functions*. NIST/Cambridge University Press.

PAPOUTSELLIS, C.E., MERCIER, M.J. & GRISOUARD, N. 2023 Internal tide generation from non-uniform barotropic body forcing. *J. Fluid Mech.* **964**, A20.

PEACOCK, T., ECHEVERRI, P. & BALMFORTH, N.J. 2008 An experimental investigation of internal tide generation by two-dimensional topography. *J. Phys. Oceanogr.* **38**, 235–242.

PETERS, F. 1985 Schlieren interferometry applied to a gravity wave in a density-stratified liquid. *Exp. Fluids* **3**, 261–269.

PÉTRÉLIS, F., LLEWELLYN SMITH, S. & YOUNG, W.R. 2006 Tidal conversion at a submarine ridge. *J. Phys. Oceanogr.* **36**, 1053–1071.

PIERCE, A.D. 1963 Propagation of acoustic-gravity waves from a small source above the ground in an isothermal atmosphere. *J. Acoust. Soc. Am.* **35**, 1798–1807.

POLLMANN, F., NYCANDER, J., EDEN, C. & OLBERS, D. 2019 Resolving the horizontal direction of internal tide generation. *J. Fluid Mech.* **864**, 381–407.

PRINSENBERG, S.J. & RATTRAY, M. 1975 Effects of continental slope and variable Brunt–Väisälä frequency on the coastal generation of internal tides. *Deep-Sea Res.* **22**, 251–263.

PRINSENBERG, S.J., WILMOT, W.L. & RATTRAY, M. 1974 Generation and dissipation of coastal internal tides. *Deep-Sea Res.* **21**, 263–281.

RAPAKA, N.R., GAYEN, B. & SARKAR, S. 2013 Tidal conversion and turbulence at a model ridge: direct and large eddy simulations. *J. Fluid Mech.* **715**, 181–209.

RATTRAY, M., DWORSKI, J.G. & KOVALA, P.E. 1969 Generation of long internal waves at the continental slope. *Deep-Sea Res.* **16 Suppl.**, 179–195.

SANDSTROM, H. 1976 On topographic generation and coupling of internal waves. *Geophys. Fluid Dyn.* **7**, 231–270.

SARKAR, S. & SCOTTI, A. 2017 From topographic internal gravity waves to turbulence. *Annu. Rev. Fluid Mech.* **49**, 195–220.

SHMAKOVA, N., ERMANYUK, E. & FLÓR, J.-B. 2017 Generation of higher harmonic internal waves by oscillating spheroids. *Phys. Rev. Fluids* **2**, 114801.

SJÖBERG, B. & STIGEBRANDT, A. 1992 Computations of the geographical distribution of the energy flux to mixing processes via internal tides and the associated vertical circulation in the ocean. *Deep-Sea Res.* A **39**, 269–291.

ST. LAURENT, L. & GARRETT, C. 2002 The role of internal tides in mixing the deep ocean. *J. Phys. Oceanogr.* **32**, 2882–2899.

ST. LAURENT, L., STRINGER, S., GARRETT, C. & PERRAULT-JONCAS, D. 2003 The generation of internal tides at abrupt topography. *Deep-Sea Res.* I **50**, 987–1003.

STIGEBRANDT, A. 1980 Some aspects of tidal interactions with fjord constrictions. *Estuarine Coastal Mar. Sci.* **11**, 151–166.

SUTHERLAND, B.R. & LINDEN, P.F. 2002 Internal wave excitation by a vertically oscillating elliptical cylinder. *Phys. Fluids* **14**, 721–731.

TABAEI, A., AKYLAS, T.R. & LAMB, K.G. 2005 Nonlinear effects in reflecting and colliding internal wave beams. *J. Fluid Mech.* **526**, 217–243.

THOMAS, N.H. & STEVENSON, T.N. 1972 A similarity solution for viscous internal waves. *J. Fluid Mech.* **54**, 495–506.

VIC, C., NAVEIRA GARABATO, A.C., GREEN, J.A.M., WATERHOUSE, A.F., ZHAO, Z., MELET, A., DE LAVERGNE, C., BUIJSMAN, M.C. & STEPHENSON, G.R. 2019 Deep-ocean mixing driven by small-scale internal tides. *Nat. Commun.* **10**, 2099.

VLASENKO, V., STASHCHUK, N. & HUTTER, K. 2005 *Baroclinic Tides. Theoretical Modeling and Observational Evidence*. Cambridge University Press.

VLASENKO, V.I. 1987 Internal wave generation in a stratified ocean of variable depth. *Izv. Atmos. Ocean. Phys.* **23**, 225–230.

VLASENKO, V.I. & CHERKESOV, L.V. 1990 The generation of baroclinic tides over steep non-uniform bottom topography. *Sov. J. Phys. Oceanogr.* **1**, 161–169.

VOISIN, B. 2020 Near-field internal wave beams in two dimensions. *J. Fluid Mech.* **900**, A3.

VOISIN, B. 2021 Boundary integrals for oscillating bodies in stratified fluids. *J. Fluid Mech.* **927**, A3.

VOISIN, B. 2024 Added mass of oscillating bodies in stratified fluids. *J. Fluid Mech.* **987**, A27.

VOISIN, B., ERMANYUK, E.V. & FLÓR, J.-B. 2011 Internal wave generation by oscillation of a sphere, with application to internal tides. *J. Fluid Mech.* **666**, 308–357.

WANG, J., CHEN, X., WANG, W. & LI, Q. 2015 Laboratory experiments on the resonance of internal waves on a finite height subcritical topography. *Ocean Dyn.* **65**, 1269–1274.

WANG, S., WANG, J., CHEN, X., MENG, J. & WANG, H. 2018 Density perturbation and energy flux of internal waves from velocity data. *J. Ocean Univ. China* **17**, 727–732.

WATSON, G.N. 1944 *A Treatise on the Theory of Bessel Functions*, 2nd edn. Cambridge University Press.

WHALEN, C.B., DE LAVERGNE, C., NAVEIRA GARABATO, A.C., KLYMAK, J.M., MACKINNON, J.A. & SHEEN, K.L. 2020 Internal wave-driven mixing: governing processes and consequences for climate. *Nat. Rev. Earth Environ.* **1**, 606–621.

WINTERS, K.B. & ARMI, L. 2013 The response of a continuously stratified fluid to an oscillating flow past an obstacle. *J. Fluid Mech.* **727**, 83–118.

WUNSCH, C. & FERRARI, R. 2004 Vertical mixing, energy, and the general circulation of the oceans. *Annu. Rev. Fluid Mech.* **36**, 281–314.

WUNSCH, C. & WUNSCH, J. 2022 Baroclinic tidal conversion: note on a paper of L.R.M. Maas. *J. Fluid Mech.* **946**, A47.

ZHANG, H.P., KING, B. & SWINNEY, H.L. 2007 Experimental study of internal gravity waves generated by supercritical topography. *Phys. Fluids* **19**, 096602.

ZHANG, L., BUIJSMAN, M.C., COMINO, E. & SWINNEY, H.L. 2017 Internal wave generation by tidal flow over periodically and randomly distributed seamounts. *J. Geophys. Res. Oceans* **122**, 5063–5074.